Modeling of coupled thermal-hydraulic-mechanical-chemical processes for predicting the evolution in permeability and reactive transport behavior within single rock fractures

AUTHOR(S):

Ogata, Sho; Yasuhara, Hideaki; Kinoshita, Naoki; Cheon, Dae-Sung; Kishida, Kiyoshi

CITATION:

Ogata, Sho ...[et al]. Modeling of coupled thermal-hydraulic-mechanical-chemical processes for predicting the evolution in permeability and reactive transport behavior within single rock fractures. International Journal of Rock Mechanics and Mining Sciences 2018, 107: 271-281

ISSUE DATE:

2018-07

URL:

http://hdl.handle.net/2433/232508

Modeling of coupled thermal-hydraulic-mechanical-chemical processes for predicting the evolution in permeability and reactive transport behavior within single rock fractures

Sho Ogata[1], Hideaki Yasuhara[2], Naoki Kinoshita[2], Dae-Sung Cheon[3] and Kiyoshi Kishida[1]

[1] Department of Urban Management, Kyoto University, Kyoto, 615-8540, JAPAN.

[2] Department of Civil and Environmental Engineering, Ehime University, Matsuyama, 790-8577, JAPAN.

[3] Korea Institute of Geoscience and Mineral Resources, Daejeon, 305-350, KOREA.

Abstract

A multi-physics numerical model was developed to predict the fluid flow and mass transport [(Re2.1)] behavior of rock fracture [(Re2.1)] under coupled thermal-hydraulic-mechanical-chemical (THMC) conditions. In particular, the model was employed for the purpose of describing the evolution of permeability and reactive transport behavior within rock fractures by taking into account the geochemical processes of the free-face dissolution and the pressure dissolution. In order to examine the capability of the developed model, the model was applied to replicate the experimental measurements of the evolution in hydraulic aperture, permeability, and element concentrations obtained from two flow-through experiments using single granite and mudstone fractures. The model predictions for the granite experiment were able to follow the actual data for the evolution in hydraulic aperture and effluent element concentrations without adopting any fitting parameters that are often used in other THMC coupled models obtained from literature. Furthermore, the model succeeded in replicating the actual changes in fracture permeability and effluent element concentrations within the mudstone fracture. Although some uncertain mismatches between the experiments and the model predictions, such as changes in the concentrations of several elements (i.e., Na and K concentrations in the granite fracture and Al in the mudstone fracture) were remaining at this stage, [(Re2.2)] the developed model should be valid for evaluating the evolution in the fluid flow and mass transport behavior within rock fracture induced by mineral dissolution under stress- and temperature-controlled conditions. [(Re2.2)]

Keywords: Coupled THMC model, Rock fracture, Permeability, Mineral dissolution, Pressure solution

Key Points:

- **A coupled THMC numerical model was developed to predict changes in the permeability and reactive transport behavior within single rock fractures.**
- **The model was validated by replicating experimental measurements using granite and mudstone fractures.**
- **There were, however, some uncertain mismatches between the experiments and the model predictions in the concentrations of several elements.**

1. Introduction

Understanding the fluid flow behavior in the deep subsurface is essential for evaluating the performance of many rock engineering projects, such as the geological disposal of high-level radioactive waste [1-3] and anthropogenic CO_2 [4], and the enhanced geothermal system (EGS) [5]. In the deep subsurface, the fluid flow behavior often depends on the hydraulic properties of the rock fracture (i.e., permeability and aperture) and the spatial distribution of the fracture network. It is well known that the permeability of fractured rocks is influenced by the coupled thermal-hydraulic-mechanical-chemical (THMC) processes under the deep geological conditions [6-8]. Among these several processes, mechanical-chemical (MC) processes, such as stress corrosion and geochemical reactions between the rock minerals and the pore water and mechanical creep, may exert a non-negligible influence on the evolution of fracture permeability [9-11]. However, within the context of the geological disposal of high-level radioactive waste, geochemical reactions, such as free-face dissolution/precipitation [12] and pressure dissolution [13-21], have been well recognized as important physical phenomena which may change the fracture permeability within a longer timescale in comparison to the mechanical processes. These processes within rock fracture often have been investigated under the hydrothermal conditions where the fluid-rock reaction is enhanced. [(Re1.2)] Robert et al. (2016) [22] conducted flow-through column-like experiments for 20 and 40 days using granite samples that have a single tensile fracture by simulating in near-field setting of shallow Enhanced Geothermal System (EGS) (i.e., 120 °C temperature, and 25-35 MPa effective stress), and fracture permeability, fracture aperture, and mass of minerals dissolved were computed through the pore-pressure observations, effluent chemistry, and X-ray CT scan imaging. Their results showed the decrease in permeability that should be due to a combination of dissolution of fracture propping asperities and mechanical creep, but finally concluded through the measurements of the effluent solution that the

permeability reduction was due to mineral dissolution of the fracture propping asperities rather than mechanical effects. Beeler et al .(2004) [23] measured the time dependent closure of fractures in quartz at 22-530°C temperature and 0.1 – 150 MPa water pressure, and reported the aperture reduction by as much as 80 % in a few hours due to a pressure dissolution-like process. Besides these observations, many other experimental studies [9-11, 24, 25] have confirmed a reduction in the permeability of rock fractures by several orders of magnitude likely due to pressure dissolution. [(Re1.2)] Therefore, in order to predict the permeability change of fractured rocks in actual fields, it should be of great importance to model the coupled THMC processes including the pressure dissolution. [(Re1.3), (Re1.5), (Re2.8)] Previous studies [9-11, 16, 18, 24] have proposed the conceptual models to predict the evolution in permeability of porous and fractured rocks due to the mechanical-chemical phenomenon (i.e., pressure dissolution). These models can describe the processes only in the representative elementary scale, and thus they can't conduct coupled THMC numerical simulations at field scales. The aim of this study is to propose a FE model that can describe coupled THMC processes including the pressure dissolution for predicting rock permeability change at the field scales. Previously, using the FE scheme we have developed a coupled THMC model incorporating the pressure dissolution at grain-to-grain contact [26]. Updating the model by incorporating the process of pressure dissolution at contacting asperities is the main purpose of this study. [(Re1.3), (Re1.5), (Re2.8)] Recent studies [25, 27-34] also have proposed several coupled THMC numerical models including the geochemical reactions (i.e., free-face dissolution and pressure solution) within rock fracture to estimate the evolution of fracture permeability. For instance, [(Re1.2)] Lang et al. (2015) [27] developed a discrete multiphysics pore-scale model by extending the direct and coupled thermo-hydro-mechanical-chemical simulation approach of the Bernabe et.al (2007) [28] from single, axisymmetric grain contacts to three-dimensional models of randomly rough, self-affine

surfaces. The model can estimate the change in fracture aperture induced by pressure dissolution and elastic compression. [(Re1.2)] However, the focus of most of these studies [27-31] has only been the development of theoretical THMC models; the studies have not verified the developed models by comparing the predictions with actual measurements obtained from experiments. In contrast, there are several studies [25, 32-34] that have developed coupled models and examined their validity by a comparison with experimental data. Yasuhara et al. (2006) [25] developed a numerical model using the Lagrangian-Eulerian method that can predict the evolution of permeability and reactive transport behavior within a single novaculite fracture by describing the geochemical reactions (i.e., free-face dissolution and pressure dissolution). This model applied additional multipliers in the calculations of the mechanical-chemical processes in order to follow the experimental measurements – the multipliers ranged from 30 to 10^6. Based on the works by Yasuhara et al [11, 25], in Task C1 of the Decovalex project, an attempt has been made to develop THMC numerical models that can reproduce the experimental measurements of single rock fractures using novaculite and granite [32-34]. In the scheme of their modeling, Bond et al. (2016) [34] and Bond et al. (2017) [33] applied some different modeling approaches, including the discretized 2D model that represents a 2D fracture surface taking the fracture topography data to locally define the fracture aperture, the homogenized (0D/1D/2D) model that treats the entire fracture surface as a single entity, and the synthetic model that uses the fracture topography data to define the statistics of the fracture aperture distribution. In their works [33,34], several participating teams attempted to apply these different modeling approaches with each team conducting calculations using their own numerical code. Most of different numerical models developed in their works [33,34] were able to replicate the experimental measurements relatively well (i.e., the evolution of fracture permeability and element concentrations), but in almost all cases, the prediction results were adjusted by incorporating the fitting parameters, called

enhancement factors and scaling factors, in the calculations of the mechanical-chemical processes with fitting parameters in the range of 245 to 10^6 [32-34].

[(Re1.3), (Re1.5), (Re2.8)] In this study, a new coupled THMC model incorporating the pressure dissolution at contacting asperities in rock fracture was developed using a FE scheme in order to predict changes in permeability of rock fracture. As mentioned above, almost of other coupled THMC models [27-31] considering the pressure dissolution within rock fracture have not been validated and several coupled THMC models [25, 32-34] need calibrations of the fitting parameters in the wide range of 30 to 10^6 [25] and 245 to 10^6 [32-34] in the calculation of mechanical-chemical process to follow the experiments, and this may not be the case for the model developed in this study – minimizing the use and the values of unknown, fitting parameters was a significant target for the model development. [(Re1.3).(Re1.5), (Re2.8)] As is obvious, in order to examine the validity of the developed model, predictions made with the model were compared with the experimental measurements obtained from flow-through experiments [11] using granite and mudstone samples.

2. Model description

2.1. Constitutive equations

The coupled THMC model developed in this work is based on the finite element scheme that can describe the interactions of multi-physics that include the heat transfer, the fluid flow,

geomechanics, and the reactive transport with the geochemical reactions of mineral dissolution/precipitation. By solving these THMC coupled processes, this model can evaluate the evolution of permeability in rock fracture. The equations for the model are presented in this section. The fluid flow in the fracture of saturated rock is simply modeled by the conservation of water mass and by assuming the Darcian flow, as follows:

$$\frac{\partial(\rho_w \phi)}{\partial t} + \nabla \cdot (\rho_w \boldsymbol{u}) = f_m, \tag{1}$$

$$\boldsymbol{u} = -\frac{\boldsymbol{k}}{\mu}(\nabla p + \rho_w g \nabla h), \tag{2}$$

$$k = \frac{b_h^{\,2}}{12}, \tag{3}$$

where ρ_w [kg m^{-3}] is the density of the fluid, ϕ [-] is the porosity, $\boldsymbol{u}$ [m s^{-1}] is the fluid velocity tensor, f_m [kg m^{-3} s^{-1}] is the source term for the flow, $\boldsymbol{k}$ [m^2] is the rock permeability tensor, μ [Pa s] is the fluid dynamic viscosity, p [Pa] is the fluid pressure, g [m s^{-2}] is the gravity acceleration, h [m] is the potential head, and b_h [m] is the hydraulic fracture aperture.

In the thermal process, the temperature of the rock is calculated by the heat transfer equation.

$$(\rho C_p)_{eq} \frac{\partial T}{\partial t} + \rho_w C_{p,w} \boldsymbol{u} \cdot \nabla T = \nabla \cdot (k_{eq} \nabla T) + Q_h, \tag{4}$$

where T [K] is the system temperature, $(\rho C_p)_{eq}$ [J K^{-1} m^{-3}] is the equilibrium volumetric heat capacity, $C_{p,w}$ [J kg^{-1} K^{-1}] is the heat capacity of the fluid, $\boldsymbol{k_{eq}}$ [W m^{-1} K^{-1}] is the equilibrium thermal conductivity tensor, and Q_h [W m^{-3}] is the heat source.

[(Re1.1),(Re1.4)] The mechanical behavior of rock structure id is calculated by the quasi-static equilibrium equation and the constitutive poroelasticity.

$$-\nabla \boldsymbol{\sigma} = \boldsymbol{F_v} \tag{5}$$

$$\boldsymbol{\sigma} = \boldsymbol{E} : (\boldsymbol{\varepsilon} - \boldsymbol{\varepsilon_T}) + \alpha_B P \boldsymbol{I} \tag{6}$$

Where $\boldsymbol{\sigma}$ [Pa] is the stress tensor, $\boldsymbol{F_v}$ [Pa m^{-1}] is the body force, $\boldsymbol{E}$ [Pa] is the elasticity tensor , $\boldsymbol{\varepsilon}$ [-] is the strain tensor, $\boldsymbol{\varepsilon_T}$ [-] is the thermal strain tensor, α_B [-] is the Biot-Willis coefficient and $\boldsymbol{I}$ [-] is the direction tensor. [(Re1.1),(Re1.4),]

The reactive transport behavior is calculated by the basic advection-diffusion equation. The mechanical dispersion and sorption processes are not considered here.

$$\frac{\partial (c_i \phi)}{\partial t} + \boldsymbol{u} \cdot \nabla c_i = \nabla \cdot (\phi \tau \boldsymbol{D}_{b,i} \nabla c_i) + r_i \,, \tag{7}$$

where c_i [mol m^{-3}] is the concentration of solute i in the pore water, ϕ [-] is the porosity, $\boldsymbol{D_{b,i}}$ [m^2 s^{-1}] is the diffusion coefficient tensor, τ [-] is the coefficient related to tortuosity, and r_i [mol m^{-3} s^{-1}] is the source term of solute i. The diffusion coefficient is temperature-dependent and can be defined by a Arhenius-type equation [35], as

$$D_{b,i} = D^0_{b,i} \exp(-E_{D,i} / RT) \,, \tag{8}$$

where $D^0_{b,i}$ [m^2 s^{-1}] and $E_{D,i}$ [J mol $^{-1}$] are the pre-exponential factor and the activation energy of the diffusion of solute i, respectively, and R [J mol $^{-1}$K^{-1}] is the gas constant.

In this work, the rock domain consists of multi-minerals. When the number of minerals included in the targeted rocks is m, the total solute source is expressed by

$$r_i = \sum_j^m \nu_i R_j \,, \tag{9}$$

where ν_i [-] is the stoichiometry coefficient of solute i in the pore water and R_j [mol m^{-3} s^{-1}] is the rate of the geochemical reactions for mineral j.

2.2. Geochemical reaction

The geochemical reaction includes free-face dissolution/precipitation and pressure dissolution. Thus, R_j is expressed by

$$R_j = R_j^{FF} + R_j^{PS}, \tag{10}$$

where R_j^{FF} and R_j^{PS} [mol m^{-3} s^{-1}] are the rates of free-face dissolution/precipitation and the pressure dissolution of mineral *j*, respectively.

Firstly, the way to estimate the rate of free-face dissolution/precipitation in rock fractures is shown. The fracture area, composed of contacting asperities and pore space, is set as the representative element (Fig. 1). The flux of the free face dissolution/precipitation per time in the representative element is represented by [12],

$$\dot{M}^{FF} = k_+ A_{rea}(1 - Q / K_{eq,}), \tag{11}$$

where $\dot{M}^{FF}$ [mol s^{-1}] is the flux of mineral *j*, induced by the free-face dissolution/precipitation per time in the representative element, k_+ [mol m^{-2} s^{-1}] is the dissolution rate constant, Q [-] is the ionic activity product, K_{eq} [-] is the equilibrium constant, A_{rea} [m^2] is the reactive surface area. The reactive surface area is obtained by a geometric relation in the representative element, given as

$$A_{rea} = 2(1 - R_c) A_t^l, \tag{12}$$

$$R_c = \frac{A_c^l}{A_t^l}, \tag{13}$$

where R_c [-] is the contact-area ratio of the fracture asperities, A_t^l [m^2] is the total fracture cross sectional area in the representative element, and A_c^l [m^2] is the contact area within the fracture of the representative element. The dissolution rate constants are defined by the Arrhenius expression, given as

$$k_{+,j} = k_{+,j}^0 \exp(-E_{k_{+,j}} / RT), \tag{14}$$

where k_{+j}^0 [mol m^{-2} s^{-1}] is the pre-exponential factor of mineral j and $E_{k_{+,j}}$ [J mol $^{-1}$] is the activation energy of the dissolution of mineral j. The volume of the pore space in the representative element is expressed by

$$V_p = (1 - R_c) A_t^l \cdot b, \tag{15}$$

where V_p[m^3] is the volume of pore space in the representative element and b[m] is the average mechanical fracture aperture. The rate of the free-face dissolution/precipitation of the rock fracture can be obtained by dividing Eq. (11) by Eq. (15), as follows:

$$R^{FF} = 2k_+(1 - Q / K_{eq}) / b. \tag{16}$$

It represents the rate of the free face dissolution/precipitation for rock composed of a single mineral. Therefore, it can be extended to that for rocks composed of multi-minerals [11]. Defining the volumetric ratio of mineral j as χ_j, and the roughness factor [36] $f_{r,j}$ of mineral j, which is the ratio of the true (microscopic) surface area over the apparent (geometric) surface area, the rate of the free-face dissolution/precipitation for mineral j is given by

$$R_j^{FF} = 2 f_{r,j} x_j k_{+,j} (1 - Q_j / K_{eq,j}) / b. \tag{17}$$

The roughness factor is calculated by the specific surface area, as follows:

$$f_{r,j} = \frac{S_j}{6/\rho_j d_j}, \tag{18}$$

where S_j [m^2 g-^{1}] is the specific surface area of mineral *j*, ρ_j [kg m^{-3}] is the density of mineral *j*, and d_j [m] is the grain diameter of mineral *j*. If the number of minerals composing the targeted rock is *n*, the total rate of the free-face dissolution/precipitation can be defined as

$$R^{FF} = \sum_j^n R_j^{FF} = \sum^n 2 f_{r,j} x_j k_{+,j} (1 - Q_j / K_{eq,j}) / b\,. \tag{19}$$

When the rock is far from the equilibrium condition, it may be possible to simplify Eq. (19) by ignoring the effect of the precipitation.

$$R^{FF} = \sum_j^n R_j^{FF} = \sum^n 2 f_{r,j} x_j k_{+,j} / b\,. \tag{20}$$

Secondly, the way to estimate the rate of pressure dissolution at the contacts within rock fractures is shown. Yasuhara et al. [9] defined the strain rate of the pressure dissolution at the contacting asperities within a fracture by evaluating the gradient of chemical potential between the contacting fracture asperities and the void space in the fracture area, given as

$$\dot{\varepsilon}^{PS} = \frac{1}{V}\frac{dV}{dt} = \frac{V_m^2 k_+}{RTb}(\sigma_a - \sigma_c)$$

$$= \frac{1}{b}\frac{\Delta b}{\Delta t} = \frac{V_m^2 k_+}{RTb}\left(\frac{\sigma_n}{R_c} - \sigma_c\right), \tag{21}$$

$$\sigma_a = \frac{\sigma_n}{R_c}, \tag{22}$$

where $\dot{\varepsilon}^{PS}$ [s^{-1}] is the strain rate of the pressure dissolution at the contacting asperities within the fracture, V_m [m^3 mol^{-1}] is the molar volume, σ_a [Pa] is the disjoining pressure [37] which is the

stress acting at the contacting asperities within the fracture, σ_c [pa] is the critical stress [35], and σ_n [Pa] is the compressive effective stress acting on the rock domain. The derived strain rate in Eq. (21) shows the uniaxial compressive state. However, under real stress conditions, the pressure dissolution may occur under triaxial compressive conditions. Therefore, it is necessary to extend Eq. (21) to the one for such conditions. The volumetric strain summing the principal strains may represent the strain induced by the pressure dissolution under the triaxial compressive conditions, and the extended strain rate may be expressed as

$$\dot{\varepsilon}^{PS} = \dot{\varepsilon}_1^{PS} + \dot{\varepsilon}_2^{PS} + \dot{\varepsilon}_3^{PS} = \frac{V_m^2 k_+}{RTb}\left(\frac{\sigma_1+\sigma_2+\sigma_3}{R_c} - 3\sigma_c\right)$$

$$= \frac{3V_m^2 k_+}{RTb}\left(\frac{\sigma_1+\sigma_2+\sigma_3}{3R_c} - \sigma_c\right)$$

$$= \frac{3V_m^2 k_+}{RTb}\left(\frac{\sigma_m}{R_c} - \sigma_c\right), \tag{23}$$

$$\sigma_m = \frac{\sigma_1+\sigma_2+\sigma_3}{3}, \tag{24}$$

where $\dot{\varepsilon}_1^{PS}$, $\dot{\varepsilon}_2^{PS}$, and $\dot{\varepsilon}_3^{PS}$ [s^{-1}] are the strain rates in the first, second, and third principal stress directions induced by the pressure dissolution, respectively, and σ_m [Pa] is the mean effective stress, σ_1, σ_2, σ_3 are the first, second, and third principal stress [Pa] . Then, the change in the averaged mechanical aperture, due to the pressure dissolution, is defined using Eq. (23).

$$\frac{\Delta b}{\Delta t} = \frac{\dot{V}^{PS}}{A_c^l} = \frac{3V_m^2 k_+}{RT}\left(\frac{\sigma_m}{R_c} - \sigma_c\right), \tag{25}$$

where $\dot{V}^{PS}$ [$m^3 s^{-1}$] is the rate of volume change by the pressure dissolution in the representative element. The rate of volume change by pressure dissolution $\dot{V}^{PS}$ is obtained by Eq. (25) and by the relation $A_c^l = R_c A_t^l$ as

$$\dot{V}^{PS} = \frac{\Delta b \cdot A_c^l}{\Delta t} = \frac{3V_m^2 k_+ R_c A_t^l}{RT}\left(\frac{\sigma_m}{R_c} - \sigma_c\right). \tag{26}$$

Accordingly, the mineral dissolution flux per time by the pressure dissolution in the representative element is defined by dividing Eq. (26) by the molar volume, as follows:

$$\dot{M}^{PS} = \frac{3V_{m,} k_+ R_c A_f^t}{RT}\left(\frac{\sigma_m}{R_c} - \sigma_c\right), \tag{27}$$

where $\dot{M}^{PS}$ [mol s^{-1}] is the flux with pressure per time in the representative element. Finally, the rate of pressure dissolution in a rock fracture is defined by dividing Eq. (27) by Eq. (15).

$$R^{PS} = \frac{3V_m k_+ R_c}{RTb(1-R_c)}\left(\frac{\sigma_m}{R_c} - \sigma_c\right). \tag{28}$$

As shown in the case of the free face dissolution/precipitation, the rate of pressure dissolution for mineral *j* is defined by using the volumetric ratio and the roughness factor of mineral *j*, given as

$$R_j^{PS} = \frac{3 f_{r,j} x_j V_{m,j} k_{+,j} R_c}{RTb(1-R_c)}\left(\frac{\sigma_m}{R_c} - \sigma_c\right), \tag{29}$$

2.3. Aperture change with geochemical reaction

Interactive processes of free face dissolution/precipitation and pressure dissolution irreversibly alter the fracture mechanical aperture, and the contact area within the fracture changes due to the change in mechanical aperture. [(Re1.6)] The relationship between the mechanical

fracture aperture and the contact area within the fracture in the representative element may be given by the following simple equation [9]:

$$b = b_r + (b_0 - b_r)\exp(-(R_c - R_{c0})/a), \tag{30}$$

where b [m] is the average mechanical fracture aperture, [(Re1.6)] b_r [m] is the residual fracture aperture, b_0 [m] is the initial fracture aperture, and a [-] is a constant. The relationship indicated by Eq. (30) is shown in Fig. 2. Constant a is an important parameter that effects the gradient of the curve.

In this work, changes in the fracture aperture are only induced by the geochemical reactions of both free face dissolution/precipitation and pressure dissolution. The rate of aperture change due to free face dissolution/precipitation and pressure dissolution in the rock fracture is defined as follows:

$$\dot{b}^{FF} = \frac{\sum_j^n M_j^{FF} \cdot V_{m,j}}{A_f^t} = \sum_j^n 2 f_{r,j} x_j (1 - R_c) k_{+,j} (1 - \frac{Q_j}{K_{eq,j}}), \tag{31}$$

$$\dot{b}^{PS} = -\frac{\sum_j^n \dot{M}_j^{PS} \cdot V_{m,j}}{A_{f,c}} = \sum_j^n \frac{3 f_{r,j} x_j k_{+,j} V_{m,j}^2 (1 - R_c)}{RT} (\frac{\sigma_m}{R_c} - \sigma_c), \tag{32}$$

where $\dot{b}^{FF}$ [m s^{-1}] is the rate of aperture change within the fracture by free-face dissolution/precipitation and $\dot{b}^{PS}$ [m s^{-1}] is the rate of aperture change within the fracture by pressure dissolution. The fracture aperture at an arbitrary time is evaluated using Eq. (33).

$$b(t) = b_0 + \int \dot{b}^{FF}(t)dt + \int \dot{b}^{PS}(t)dt, \tag{33}$$

where b_0 [m] is the initial fracture aperture. Once the mechanical fracture aperture is calculated, the hydraulic fracture aperture is also evaluated by using the following relationship [38, 39] between the hydraulic fracture aperture and the mechanical fracture aperture:

$$b_h^3 = \frac{(1-R_c)}{(1+R_c)} b^3, \tag{34}$$

[(Re1.7)] In this work, the COMSOL Multiphysics [40] is used to solve the differential equations. The calculation procedure of model is shown in Fig. 3. Using the scheme that the dependent variables (i.e., fracture aperture /permeability, flow velocity, stress, temperature, and dissolution/precipitation rate constants) are exchanged reciprocally, the coupled THMC processes are calculated sequentially. [(Re1.7)]

3. Model verification

3.1. Replicating experimental measurements

In order to verify the model proposed in the previous section, an attempt is made to replicate the experimental results by the model. The experiments that are targeted for the numerical analysis are the flow-through experiments conducted on the granite and mudstone samples [11]. Rock samples which have a single artificial fracture, shown in Fig. 4, are used for the experiments. The experimental setup is also shown in this figure. [(Re1.8)] Two experiments, namely, E-3 and H-11, are conducted with samples of the granite (30 mm in diameter × 60 mm in length) and mudstone (50 mm in diameter × 100 mm in length), respectively. E-3 is conducted using

deionized water (pH ~7) as the permanent at confining pressures of 5.0 MPa, time dependent temperatures of 25 and 90°C (0-380 h: 25°C, after 380 h: 90°C) and at differential water pressure levels ranging from 0.04 to 0.10 MPa. Similarly, H-11 is conducted using deionized water (pH ~6) at confining pressure of 3.0 MPa, temperatures of 90°C, and at differential water pressure of 0.4 MPa. In two experiments, hydraulic aperture is obtained from the measured flow rate via parallel plate approximation, as follows:

$$<b_h>=\left(\frac{12\mu l Q}{w\Delta P}\right)^{1/3} \quad (35)$$

Q [m^3 s^{-1}] is the measured flow rates, ΔP [Pa] is differential pressure, $<b_h>$ [m] is the equivalent hydraulic aperture, w [m] is width of the sample, l [m] is the length of the sample. The concentrations of effluent element (Si, Al, K, Fe, Ca, Na, and Mg) are obtained by examining the compositions of fluid samples taken from the flow outlet in two experiments using inductively-coupled plasma atomic emission spectrometry (ICP-AES). [(Re1.8)] The chemical compositions of the granite and mudstone used for the experiments are listed in Table 1 [11].

[(Re1.9), (Re2.5)] The numerical calculations using the coupled THMC model presented in this work are conducted to reproduce the experimental measurements of evolution in hydraulic fracture aperture and effluent element concentrations for experiments of granite (E-3) and mudstone (H-11). The numerical domains that represent the rock fracture of samples in two dimensions are set to be rectangles with width of 30 mm and length of 60mm (E-3) and with width of 50 mm and length of 100mm (H-11), and these domains for E-3 and H-11 are divided into 1800 and 5000 square elements, respectively (Fig. 5). In the models of E-3 and H-11, the

316 equivalent values are applied as the initial hydraulic aperture and contact-area ratio within the
317 whole domains. The values of initial hydraulic aperture are obtained from experimental
318 measurements of E-3 and H-11. As noted in Yasuhara and Elsworth (2006) [25], the values of
319 initial contact-area ratio, residual aperture and constant *a* should be derived by evaluating the
320 relation represented in Eq. (30) from experimental measurements. [(Re1.10)] However, the
321 relation is not obtained in two experiments of E-3 and H-11, so the initial contact-area ratio,
322 residual aperture, and constant *a* are assumed equivalent to those defined by Yasuhara et al. (2011)
323 [11]. [(Re1.10)] The critical stresses are assumed to be 100 MPa and 15 MPa for E-3 and H-11,
324 which are closely equivalent to their uniaxial compressive strength, respectively. Isothermal
325 condition within the whole domains changes from 25°C to 90°C by corresponding to the
326 experimental period for E-3 and is invariant of 90 °C for H-11, respectively. All the element (Si,
327 Al, K, Fe, Ca, Na, Mg) concentrations of 0 mol m^{-3} are prescribed as the initial condition within
328 the domain and as fixed concentration condition of the inflow boundary for E-3 and H-11.
329 [(Re1.1)] In the calculation of geochemical reactions, the model uses the Eq.(20) that assumes
330 that the dissolved mineral concentrations are far from equilibrium based on the experimental
331 observations [11]. Therefore, the concentrations of each element depend only on time and
332 temperature and are calculated via the simple rate law of Eq. (20). [(Re1.1)] The differential
333 pressures ranging from 0.04-0.1 MPa and that of 0.4 MPa are set in the inlet and outlet boundary

of the domain for E-3 and H-11, respectively. The mass of water and chemical species are obtained at the outlet boundary. In all models, effective stress analysis is conducted by considering both confining pressure and water pressure distribution and thermal expansion of rock structure is not considered. [(Re1.9), (Re2.5)] In the numerical analysis for the granite experiment, E-3, five minerals, namely, quartz (50 vol.%), orthoclase (20 vol.%), albite (8.0 vol.%), anorthite (20 vol.%), and biotite (2.0 vol.%), are considered [11]. In the case of the mudstone experiment, six minerals, namely, quartz (10 vol.%), orthoclase (10 vol.%), albite (15 vol.%), Illite (13 vol.%), smectite (12 vol.%), and Opal-CT (40 vol.%), are considered [41]. In the predictions for the granite experiment, it is assumed that the surface roughness of the rock fracture is equivalent to that of the minerals composing the rock. Therefore, in all the predictions, the roughness factors of the minerals composing the granite (see Eq.(18)) are estimated using the specific surface area of the granite-ground particles measured by the BET method [11]. However, the roughness factor of biotite is calculated using only the specific surface area of the biotite itself, obtained from the literature [42], because it is much greater than the specific surface areas of the other four minerals (i.e., quartz, orthoclase, albite, and anorthite). For the granite experiment, the roughness factor of the quartz, orthoclase, albite, and anorthite is 7.12 [11] and that of biotite is 512 [42]. Similarly, in the case of the mudstone predictions, the roughness factors of the minerals composing the mudstone are also estimated using the specific surface area of the mudstone-ground particles

352 measured by the BET method, but those of illite and smectite are calculated using the values
353 obtained from the literature [43]. For the mudstone experiment, the roughness factor of the quartz,
354 orthoclase, albite, and Opal-CT is 219 and that of illite and smectite are 513 and 1860,
355 respectively [43]. The parameters of the kinetic dissolution rate constant (see Eq. (14)) for the
356 minerals considered in the calculations obtained from literature are given in Table 2 [44-50].
357 Furthermore, each calibrations of the parameters used in the analysis are shown in Table 3 [11,
358 35,42-50].

359

360 **3.2. Comparisons with experimental measurements**

361 In the numerical analysis for the granite experiment, E-3, the predictions of the evolution in
362 hydraulic aperture and effluent element concentrations obtained from the experimental results
363 were made with the model. These predictions were obtained by utilizing different values for the
364 uncertain parameter, a (=0.02, 0.03, and 0.04), in the relation between the aperture and the
365 contact-area ratio (Eq. (30)) to evaluate the influence on changes in the hydraulic aperture and
366 element concentrations.

367 A comparison of the change in hydraulic aperture between the experimental results and the
368 predictions for E-3 is shown in Fig. 6. When the temperature is 25°C (i.e., 0 - 380 h), the
369 predictions with a of 0.03 and 0.04 can replicate the experimental data. After increasing the
370 temperature from 25°C to 90°C, predictions with a of 0.02 and 0.03 follow the experimental

results relatively well. In particular, among the three cases, the prediction with *a* of 0.03 is the most congruent with the measurements throughout the experimental period.

Predictions of the evolution in concentrations for the seven elements for E-3 are shown in Fig. 7, together with the corresponding experimental data. The predicted changes in concentrations for five elements (i.e., Si, Al, Fe, Ca, and Mg), except for K and Na, are similar to the measurements. The K and Na concentrations are underestimated by the predictions. In the case of the K concentration, the difference between the experiments and the predictions is relatively small. However, in the case of the Na concentration, the gap is relatively significant, and this is unexplainable at this stage. Although there are some differences between the experiments and the predictions, the current model can predict the evolution of the concentrations for most elements. The relationships in each element concentration, between the measurements and the predictions with a=0.03, are shown in Fig. 8. This figure shows that the predicted concentrations for four elements (i.e., Al, Fe, Ca, and Mg) coincide well with the measurements for the other elements.

All the results for the comparisons between the predictions and the experimental results for E-3 indicate that the current model can replicate changes in the hydraulic aperture and concentrations within the granite fracture due to the geochemical reactions (i.e., free-face dissolution and pressure dissolution) only by tuning uncertain parameter *a*. Previous works [11, 28], which make predictions of the experimental measurements for E-11 by numerical models, conclude that it is difficult to replicate the evolution in element concentrations only by the simple parameterizations (i.e., tuning of the parameter, namely, *a* in this work) for geochemical reactions. For example, Bond et al. [28] utilized fitting parameters, called “rate enhancement factors”, ranging widely from 245 to 10^6 for adjusting the rates of free-face dissolution and pressure

394 dissolution. [(Re2.11)] In contrast, the current model shown in this work can replicate the
395 experiments without these fitting parameters used in the model [28]. [(Re2.11)]

396 In the numerical analysis for the mudstone experiment, H-11, the predictions of evolution in
397 rock permeability and effluent element concentrations obtained from the experimental results
398 were made with the model. In these predictions, three kinds of uncertain parameter *a*, namely,
399 0.06, 0.07, and 0.08, were utilized. Predictions of the evolution in rock permeability for H-11 are
400 shown in Fig. 9, together with the experimental data. Each prediction with three kinds of *a* (=0.06,
401 0.07, and 0.08) slightly underestimates the experimental measurements, but they are relatively
402 congruent with the measurements taken throughout the experimental period. In particular, among
403 the three cases, the prediction with *a* of 0.06 coincides the best with the measurements.

404 The predicted changes in concentrations for the seven elements for H-11 are shown in Fig.
405 10, together with the corresponding experimental data. The trends in evolution for the element
406 concentrations are different between the experiments and the predictions. In the experiments, the
407 concentrations generally decrease with time, while the predicted concentrations increase with time.
408 In experiment H-11, the fracture surfaces of the mudstone sample were not washed with water
409 before initiating the flow. Thus, fine particles might have remained on the surfaces, and the
410 detection of the dissolution of the fine particles might have caused the higher concentrations
411 observed in the early experimental period. This was not considered in the predictions.
412 Consequently, in actual data, the element concentrations are the highest at the beginning of the
413 experiments and they decrease monotonically with time. After 200 h in the experiment, the
414 observed concentrations are likely to be steady. This implies that the dissolution of the fine
415 particles is completed within 200 h and that the dissolution of the rock itself (i.e., free face
416 dissolution and pressure dissolution) becomes dominant. Once again, in the current model, the

417 above-mentioned mechanism is not taken into account and the predictions are mismatched with
418 the actual data in the early experimental period. However, the predicted concentrations begin to
419 approach the experimental measurements after 200 h. The predictions of concentrations for five
420 elements (i.e., Si, K, Fe, Ca, and Mg), except for Al and Na, follow the measurements well after
421 200 h. In particular, the predicted Si concentration is in good agreement with the actual
422 measurements. Comparisons of each element concentration between the measurements and the
423 predictions, with a = 0.06 for the whole experimental period and for that after 200 h, are shown in
424 Figs. 11a and 11b, respectively. The mismatches between the measurements and the predictions
425 are apparent from Fig. 11a, but somewhat better agreements, except for Al, are obtained for the
426 predictions after 200 h (Fig. 11b). Only the Al concentration is significantly overestimated by the
427 prediction during most of the experimental period. This mismatch may be the result of an
428 unaccounted contribution of the precipitation at the fracture void walls, which should be further
429 examined.

430 All the results of the comparisons between the predictions and the experimental
431 measurements for H-11 indicate that the current model can follow the evolution in rock
432 permeability and element concentrations within the mudstone fracture, resulting in the fact that
433 the dominant mechanism of the permeability change should be a convolved phenomenon of the
434 free face dissolution and pressure dissolution. Overall, a comparison between the results of the
435 numerical analysis and the experiments for E-3 and H-11 provides confidence and support for the
436 use of the current model for evaluating the evolution in flow and transport behavior within rock
437 fractures due to the free face dissolution and the pressure dissolution, depending on the applied
438 stress and temperature conditions.

439

4. Conclusion

A coupled THMC model was developed based on the finite element scheme to evaluate the evolution of permeability and reactive transport behavior in fractured rocks at field scale. The model can describe the interactions of the multi-components including heat transfer, fluid flow, the variation in stress distribution, and the reactive transport with geochemical reactions (i.e., the free-face dissolution and pressure dissolution). In order to verify the developed model, the model was applied to replicate the experimental results of the changes in hydraulic aperture, fracture permeability, and element concentrations obtained from flow-through experiments conducted on granite and mudstone samples with a single artificial fracture. [(Re2.11)] The predictions for the granite and mudstone experiments showed that the model can replicate the evolution in hydraulic aperture, fracture permeability and effluent element concentrations by a simple parameterization (i.e., adjustment of the parameter "*a*" in Eq. (30)). Previous coupled THMC models [25, 32-34] need calibrations using the fitting parameters ranging widely from 30 to 10^6 [25] and 245 to 10^6 [32-34] in the calculation of geochemical reactions to follow the experiments, but our model presented in this study can replicate the experimental measurements without the fitting parameters. So, the developed model requires less calibration than the previous models [25, 32-34]. [(Re2.11)] From the analysis results obtained in this work, it can be concluded that the current model should be valid for evaluating the evolution in fluid flow and mass transport behavior within rock fracture under the coupled thermal-hydraulic-mechanical-chemical conditions that may enhance the geochemical reactions of free-face dissolution and pressure dissolution. However, some unpredictable behaviors, such as the evolution in the concentrations of Na and K elements for the granite experiment and that of the Al element concentration for the mudstone experiment, still

exist at this stage. Thus, further detailed investigations into the reactive transport behavior due to the geochemical process are required.

Acknowledgments

This work was supported by JSPS KAKENHI, Grant No. 26249139, and by the Basic Research and Development Project of the Korea Institute of Geoscience and Mineral Resources (KIGAM, Project Code No. GP2015-010), which was funded by the Ministry of Science, ICT & Future Planning, Korea. Their support is gratefully acknowledged. The data used in this work are available from the authors upon request.

Nomenclature [(Re1.7)]

A_{rea}	reactive surface area [m^2]
A_t^l	total fracture cross sectional area in the representative element [m^2]
A_c^l	contact area within the fracture of the representative element [m^2]
a	constant [-]
b	average mechanical fracture aperture [m]
b_r	residual fracture aperture [m]
b_0	initial fracture aperture [m]
b_h	hydraulic fracture aperture [m]
$\dot{b}^{FF}$	rate of aperture change within the fracture by free-face dissolution/precipitation [m s^{-1}]
$\dot{b}^{PS}$	rate of aperture change within the fracture by pressure dissolution [m s^{-1}]
c_i	concentration of solute *i* in the pore water [mol m^{-3}]
$C_{p,w}$	heat capacity of the fluid [J kg^{-1} K^{-1}]
$\boldsymbol{D_{b,i}}$	diffusion coefficient tensor [m^2 s^{-1}]
d_j	grain diameter of mineral *j* [m]

488	$\boldsymbol{E}$	elasticity tensor [Pa]
489	$E_{D,i}$	activation energy of the diffusion of the solute *i* [J mol^{-1}]
490	$E_{k+,j}$	activation energy of dissolution of mineral *j* [J mol^{-1}]
491	$\boldsymbol{F_v}$	body force [Pa m^{-1}]
492	f_m	source term for flow [kg m^{-3} s^{-1}]
493	$f_{r,j}$	roughness factor of mineral *j*[-]
494	g	gravity acceleration [m s^{-2}]
495	h	potential head of the fluid [m]
496	$\boldsymbol{I}$	direction tensor [-]
497	$K_{eq,j}$	equilibrium constant of mineral *j* [-]
498	$\boldsymbol{k}$	rock permeability tensor [m^2]
499	$\boldsymbol{k_{eq}}$	equilibrium thermal conductivity tensor [W m^{-1} K^{-1}]
500	k_+	dissolution rate constant [mol m^{-2} s^{-1}]
501	$\dot{M}^{FF}$	The flux of the free face dissolution/precipitation per time in the
502		representative element [kg m^{-3} s^{-1}]
503	$\dot{M}^{PS}$	flux with pressure dissolution per time in the representative element
504		in the representative element [kg m^{-3} s^{-1}]
505	p	fluid pressure [Pa]
506	Q	ionic activity product [-]

507	Q_h	heat source [W m^{-3}]
508	R	gas constant [J mol^{-1} K^{-1}]
509	R_c	contact-area ratio of fracture asperities [-]
510	R_j^{FF}	rate of the free face dissolution/precipitation for mineral *j* [mol m^{-3} s^{-1}]
511	R_j^{PS}	rate of pressure dissolution for mineral *j* [mol m^{-3} s^{-1}]
512	R_j	rate of the geochemical reactions for mineral *j* [mol m^{-3} s^{-1}]
513	r_i	source term of solute *i* [mol m^{-3} s^{-1}]
514	S_j	specific surface area of mineral *j* [m^2 g-^{1}]
515	T	system temperature [K]
516	$\boldsymbol{u}$	fluid velocity tensor [m s^{-1}]
517	V_p	volume of pore space in the representative element [m^3]
518	$\dot{V}^{PS}$	rate of volume change by the pressure dissolution in the representative
519		element [m^3 s^{-1}]
520	V_m	molar volume [m^3 mol^{-1}]
521		
522	*Greek letters*	
523	α_B	Biot-Willis coefficient [-]
524	$\boldsymbol{\varepsilon}$	strain tensor [-]
525	$\boldsymbol{\varepsilon_T}$	thermal strain tensor [-]

526	$\dot{\varepsilon}_1^{PS}$	strain rates in the first principal stress directions induced by the
527		pressure dissolution [s^{-1}]
528	$\dot{\varepsilon}_2^{PS}$	strain rates in the second principal stress directions induced by the
529		pressure dissolution [s^{-1}]
530	$\dot{\varepsilon}_3^{PS}$	strain rates in the third principal stress directions induced by the
531		pressure dissolution [s^{-1}]
532	$\dot{\varepsilon}^{PS}$	strain rate of the pressure dissolution at the contacting asperities within
533		the fracture [s^{-1}]
534	ϕ	porosity [-]
535	μ	fluid dynamic viscosity [Pa s]
536	ρ_j	density of the mineral *j* [kg m^{-3}]
537	ρ_w	density of the fluid [kg m^{-3}]
538	$(\rho C_p)_{eq}$	equilibrium volumetric heat capacity [J K^{-1} m^{-3}]
539	v_i	stoichiometry coefficient of solute *i* in the pore water
540	χ_j	volumetric ratio of mineral *j* [-]
541	$\boldsymbol{\sigma}$	stress tensor [Pa]
542	σ_a	stress acting at the contact area [Pa]
543	σ_c	critical stress [Pa]

544 σ_m mean effective stress [Pa]

545 σ_n compressive effective stress acting on the rock domain [Pa]

546 σ_1 first principal stress [Pa]

547 σ_2 second principal stress [Pa]

548 σ_2 third principal stress [Pa]

549 τ tortuosity [-]

550

551

552

References

[1] Tsang CF, ed. Coupled Processes Associated with Nuclear Waste Repositories. Amsterdam: Elsevier; 2012.

[2] Tsang Y. Effects of coupled processes on a proposed high-level radioactive waste repository at Yucca Mountain, Nevada. Geol Soc Am Memoirs. 2012; 209: 363–393.

[3] Rutqvist J, Wu Y-s, Tsang C-F, et al. A modeling approach for analysis of coupled multiphase fluid flow, heat transfer, and deformation in fractured porous rock. Int J Rock Mech Min Sci 2002; 39: 429-42.

[4] Zhang R, Yin X, Winterfeld PH, Wu Y-S. A fully coupled thermal-hydrological-chemical model for CO_2 geological sequestration. J Nat Gas Sci Eng. 2016; 28: 280-304.

[5] Hunsbedt A, Kruger P, London AL. Recovery of energy from fracture simulated geothermal reservoirs. J Petrol Tech 1977; 29: 940-6.

[6] Nasir O, Fall M, Evgin E. A simulator for modeling of porosity and permeability changes in near field sedimentary host rocks for nuclear waste under climate changes influences. Tunnel Underground Space Technol. 2014; 42: 122-135.

[7] Danko G, Bahrami D. A New T-H-M-C Model Development for Discrete-Fracture EGS studies, GRC Transactions, 2012; 36: 383-392.

[8] Ghassemi A. A review of some rock mechanics issues in geothermal reservoir development. Geotech.Geol. Eng. 2012; 30: 647-664.

[9] Yasuhara H, Elsworth D, Polak A. Evolution of permeability in a natural fracture: the significant role of pressure solution. J Geophys Res. 2004; 109(B3): B03204 http://dx.doi.org/10.1029/2003JB002663.

[10] Yasuhara H, Elsworth D. Compaction of a rock fracture moderated by competing roles of stress corrosion and pressure solution. Pure Appl Geophys. 2008; 165: 1289–1306.

[11] Yasuhara H, Kinoshita N, Ohfuji H, Lee DS, Nakashima S, Kishida K. Temporal alteration of fracture permeability in granite under hydrothermal conditions and its interpretation by coupled chemo-mechanical model. Appl Geochem. 2011; 26: 2074–2088.

[12] Lasaga AC. Chemical kinetics of water-rock interactions. J Geophys Res.1984; 89: 4009–4025.

[13] Wely PK. Pressure solution and force of crystallization: a phenomenological theory. J Geophys Res. 1959; 64: 2001-2025.

[14] Rutter EH. The kinetics of rock deformation by pressure solution. Philos Trans Roy Soc London Ser. 1976; A283: 203-219.

[15] Raj R. Creep in polycrystalline aggregates by matter transport through a liquid phase. J Geophys Res. 1982; 87: 4731-4739.

588 [16] Robin P-YF. Pressure solution at grain to grain contacts. Geochim Cosmochim Acta.1978;
589 42: 1383-1389.
590 [17] Zhang X, Spies CJ, Peach CJ. Compaction creep of wet granular calcite by pressure solution
591 at 28-150℃. J Geophys Res. 2010; 115(B9): B09217.
592 [18] Yasuhara H, Elsworth D, Polak A. A mechanistic model for compaction of granular
593 aggregates moderated by pressure solution. J Geophys Res. 2003; 108(11): 2530
594 http://dx.doi.org/10.1029/2003JB002536.
595 [19] Zubtsov S, Renard F, Gratier JP, Guiguet R, Dysthe DK, Traskine V. Experimental pressure
596 solution compaction of synthetic halite/calcite aggregates. Tectonophysics. 2004; 385: 45-57.
597 [20] Nenna F, Aydin A. The formation and growth of pressure solution seams in clastic rocks: A
598 field and analytically study. J Struct Geol. 2011; 33: 633-643.
599 [21] Fowler AC, Yang X. Pressure solution and viscous compaction in sedimentary basins. J
600 Geophys Res. 1999; 104(B6): 12989-12997.
601 [22] Robert A C, EhsanG, Julia NP, Nico P. Experimental investigation of fracture aperture and
602 permeability change within Enhanced Geothermal Systems. Geothermics. 2016; 62: 12–21.
603 [23] Beeler MN, Hickman SH. Stress-induced, time-dependent fracture closure at hydrothermal
604 conditions. J Geophys Res. 2004; 109(B3): B02211 doi:10.1029/2002JB001782.
605 [24] Yasuhara H, Elsworth D, Polak A, Liu J, Grader A, Halleck P. Spontaneous permeability
606 switching in fractures in carbonate: lumped parameter representation of mechanically and
607 chemically mediated dissolution. Transp Porous Media. 2006; 65: 385–409.
608 [25] Yasuhara H, Elsworth D.A numerical model simulating reactive transport and evolution of
609 fracture permeability. Int J Numer Anal Mech Geomech. 2006; 30: 1039-1062.
610 [26] Yasuhara, H., N. Kinoshita, S. Ogata, D. S. Cheon, and K. Kishida. 2016. Coupled
611 thermo-hydro-mechanical-chemical modeling by incorporating pressure solution for
612 estimating the evolution of rock permeability, Int. J. Rock Mech. Min. Sci. 86:104-114.
613 [27] Lang PS, Paluszny A, Zimmerman RW. Hydraulic sealing due to pressure solution contact
614 zone growth in siliciclastic rock fractures. J Geophys Res: Solid Earth. 2016; 120(6): 4080–
615 4101. http://doi.org/10.1002/2015JB011968.
616 [28] Bernabe Y, Evans B. Numerical modeling of pressure solution deformation at axisymmetric
617 asperities under normal load. Geol. Soc. London Spec. Publ. 2014; 284:185-205.
618 doi:10.1144/SP284.13.
619 [29] Taron J, Elsworth D. Coupled mechanical and chemical processes in engineered geothermal
620 reservoirs with dynamic permeability. Int J Rock Mech Mi Sci.2010; 47: 1339-1348.
621 [30] Taron J, Elsworth D, Min KB. Numerical simulation of
622 thermal-hydrologic-mechanical-chemical processes in deformable fractured media. Int J Rock
623 Mech Min Sci. 2009; 46(5): 842-854.

[31] Zhang Y-J, Yan C-S, Xu G. FEM analysis for T-H-M-M coupling processes in dual porosity rock mass under stress corrosion and pressure solution. J Appl Math, 2012; Article ID 983718: 21. doi: 10.1155/2012/983718.

[32] McDermott C, Bond A, Harris AF, Chittenden N, Thatcher K. Application of hybrid numerical and analytical solutions for the simulation of coupled thermal, hydraulic, mechanical and chemical processes during fluid flow through a fractured rock. Environ Earth Sci. 2015; 74: 7837-7854.

[33] Bond A, Brusky I, Chittenden N, Feng X-T, Kolditz O, Lang P, Lu R, McDermott C , Neretnieks I, Pan P-Z, Sembera J, Shao H, Yasuhara H. Development of approaches for modelling coupled thermal–hydraulic–mechanical–chemical processes in single granite fracture experiments. Environ Earth Sci. 2016; 75: 1313.

[34] Bond A, Brusky I, Cao T, Chittenden N, Fedors R, Feng X-T, Gwo J-P, Kolditz O, Lang P, McDermot C, Neretnieks I, Pan PZ, Sembera J, Shao H, Watanabe N, Yasuhara H, Zheng H. A synthesis of approaches for modeling coupled thermal-hydraulic-mechanical-chemical process in a single novaculite fracture experiment. Environ Earth Sci. 2017; 76: 12.

[35] Revil A. Pervasive pressure-solution transfer a poro-visco-plastic model. Geophys Res Lett. 1999; 26: 255–258.

[36] Murphy WM, Helgeson HC. Thermodynamic and kinetic constraints on reaction rates among minerals and aqueous solutions. IV. Retrieval of rate constants and activation parameters for the hydrolysis of pyroxene, wollastonite, olivine, andalusite, quartz, and nepheline. Am. J. Sci. 1989; 289: 17–101.

[37] Heidug WK. Intergranular solid-fluid phase transformations under stress: the effect of surface forces. J Geophys Res. 1995; 100: 5931–5940.

[38] Walsh J. Effect of pore pressure and confining pressure on fracture permeability. Int J Rock Mech Min Sci Geomech. 1981; 18(5): 429–435.

[39] Bond A. Task C1 final report. KTH Report ISBN 978-91-7595-829-3(06).2016; ISSN 1650-86-10. http://www.decovalex.org/resources.html#reports.

[40] COMSOL2014 : COMSOL MULTIPHYSICS. Version 5.0, Available from www.comsol.com.

[41] Ochhs M, Tachi Y, Trudel D, Suyama T. Kd Setting Approaches for Horonobe Mudstone Systems: Applications of TSMs and Semi-quantitative Estimation Procedures. JAEA-Research. 2012; 44: 147.

[42] Kalinowski BE, Schweda P. Kinetics of muscovite, phlogopite, and biotite dissolution and alternation at pH 1-4, room temperature. Geochim. Cosmochim. Act. 1996; 60: 367-385.

[43] Macht F, Eusterhues K, Pronk JG, Totsche UK. Specific surface area of clay minerals: composition between atomic force microscopy measurements and bulk-gas (N2) and –liquid (EGME) adsorption methods. Appl. Clay Sci. 2011; 53: 20-26.

[44] Acker JG, Bricker OP. The influence of pH on biotite dissolution and alternation kinetics at low temperature. Geochem. Cosmochim. Acta. 1992; 56: 3073-3092.

[45] Chou L, Wollast R. Study of weathering of albite at room temperature and pressure with a fluidized bed reactor. Geochem. Cosmochim. Acta. 1984; 48: 2205-2217.

[46] Helgeson HC, Murphy WM, Aagaard P. Thermodynamic and kinetic constraints on reaction rates among minerals and aqueous solutions. II. Rate constants, effective surface area, and the hydrolysis of feldspar. Geochim. Cosmochim. Acta. 1984: 48: 2405–2432.

[47] Hellman R. The albite-water system: Part I. The kinetics of dissolution as a function of pH at 100, 200, and 300 C. Geochim. Cosmochim. Acta. 1994; 58: 595–611.

[48] Oelkers E.H, Schott J. Experimental study of anorthite dissolution and the relative mechanism of feldspar hydrolysis. Geochim. Cosmochim. Acta. 1995; 59: 5039–5053.

[49] Tester JW, Worley WG, Robinson BA, Grigsby CO, Feerer JL. Correlating quartz dissolution kinetics in pure water from 25 to 625°C. Geochim. Cosmochim. Acta 1994; 58: 2407–2420.

[50] Palandri JL, Kharaka YK. A compilation of rate parameters of mineral-water interaction kinetics for application to geochemical modelling. US Geological Survey open file report. 2004; 2004–1068.

List of Tables

Table 1. Composition of granite and mudstone [11].

Oxide	Granite results (wt %)	Mudstone results (wt %)
SiO_2	65.47	71.2
Al_2O_3	11.56	10.7
K_2O	7.39	2.78
Fe_2O_3	6.24	6.78
CaO	3.75	1.66
Na_2O	3.40	1.51
TiO_2	0.55	0.876
MgO	0.54	1.51
MnO	0.24	
SO_3		3.26
Others	0.66	0.48

698 Table 2. The parameters of the kinetic dissolution rate constant for the minerals [44-50].

Mineral	Chemical formula	Molar volume (m^3 mol^{-1})	Pre-exponential factor [mol m^{-2} s^{-1}]	Activation energy (kJ mol^{-1})
Quartz	SiO_2	2.27×10^{-5}	276	90
Orthoclase	$KAlSi_3O_8$	1.09×10^{-4}	1.28×10^{-5}	38.0
Albite	$NaAlSi_3O_8$	1.00×10^{-4}	3.91×10^{-4}	50.7
Anorthite	$CaAl_2Si_2O_8$	1.01×10^{-4}	9.97×10^{-7}	17.8
Biotite	$K\ Mg_{2.5}Fe_{0.5}AlSi_3O_{10}(OH)_{1.75}F_{0.25}$	1.40×10^{-4}	1.01×10^{-7}	22.0
Cristobalite	SiO_2	2.59×10^{-5}	1.20×10^{-1}	65.0
Smectite	$K_{0.04}Ca_{0.5}(Al_{02.8}Fe_{0.53}Mg_{0.7})(Si_{7.65}Al_{0.35})O_{20}(OH)_4$	3.22×10^{-4}	4.64×10^{-5}	49.4
Illite	$(Ca_{0.01}Na_{0.13}K_{0.53})(Al_{1.27}Fe_{0.36}Mg_{0.44})(Si_{3.55}Al_{0.45})O_{10}(OH)_2$	1.48×10^{-4}	4.64×10^{-5}	49.4

699

700

701

702

703

704

705

706

707 Table 3. Calibration of the parameters used in the analysis [11,35, 42-50]. [(Re1.7)]

Parameters	Calibrations
System temperature T	Equivalent to experimental conditions of E-3 [11] and H-11
Diffusion coefficient $D_{b,i}$	Eq.(16) with literature [35]
Initial aperture b_0	Experimental measurements of E-3[11] and H-11
Initial contact area ratio R_{c0}	Equivalent to that defined by Yasuhara et al. (2011) [11]
Residual aperture b_r	Equivalent to that defined by Yasuhara et al. (2011) [11]
Critical stress σ_c	Closely equivalent to uniaxial compressive strength
Constant a	Closely equivalent to that defined by Yasuhara et al. (2011) [11]
Roughness factor $f_{r,j}$	Eq.(16) with literature [11,42,43]
Kinetic dissolution rate constants $k_{+,j}$	Eq.(12) with literature [44-50]

708

709

710

711

712

713

714 **List of Figures**

715 Fig. 1. Geometrical model that includes representative element in rock fracture area [11].
716 Tributary area A_t^l (center) is the representative element composed of asperity contact area
717 $R_c A_t^l$, and pore space (right side).

718 Fig. 2. Relation between fracture aperture and contact area ratio [11].

719 Fig. 3. Sequential procedure to conduct consistent calculations of aperture change with time.

720 Fig. 4. Schematic of flow-through experiment (left side) and rock samples (right side) [11].

721 Fig. 5. Model geometry for analysis of E-3 and H-11

722 Fig. 6. Comparisons of evolution in fracture aperture (E-3) between measurements and
723 predictions with different values for *a* used in Eq. (28).

724 Fig. 7. Comparisons of element concentrations (E-3) between measurements and predictions ((a)
725 Si, (b) Al, (c) K, (d) Fe, (e) Ca, (f) Na, and (g) Mg).

726 Fig. 8. Comparisons of element concentrations (E-3) between measurements and predictions with
727 a=0.03 used in Eq. (28).

728 Fig. 9. Comparisons of evolution of fracture aperture (H-11) between measurements and
729 predictions with different values for *a* used in Eq. (28).

730 Fig. 10. Comparisons of element concentrations (H-11) between measurements and predictions
731 with different values for *a* used in Eq. (28) ((a) Si, (b) Al, (c) K, (d) Fe, (e) Ca, (f) Na,
732 and (g) Mg).

733 Fig. 11. Comparisons of element concentrations (H-11) between measurements and predictions
734 with $a = 0.06$ used in Eq. (28): (a) for whole experimental period and (b) for
735 experimental period after 200 h.

736

737

738

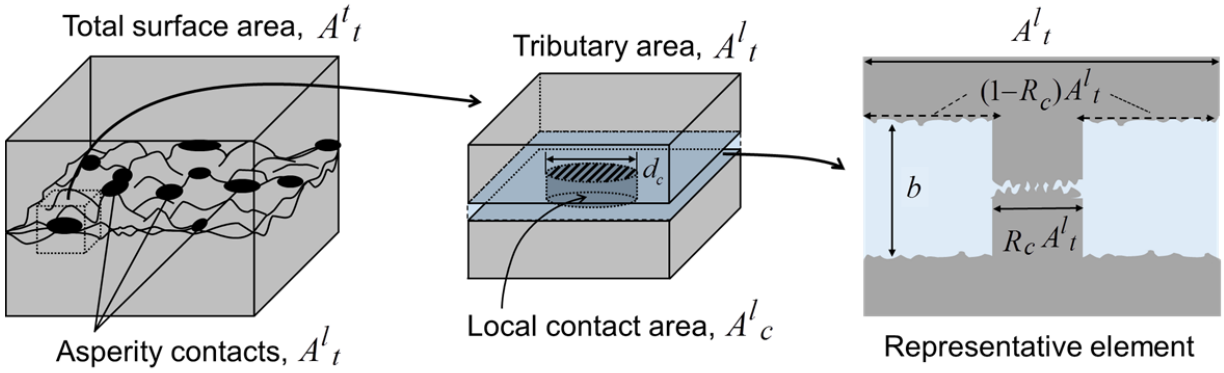

739

740 Fig. 1. Geometrical model that includes representative element in rock fracture area [11].

741 Tributary area $A^l{}_t$ (center) is the representative element composed of asperity contact area $R_c A^l{}_t$,

742 and pore space (right side).

743

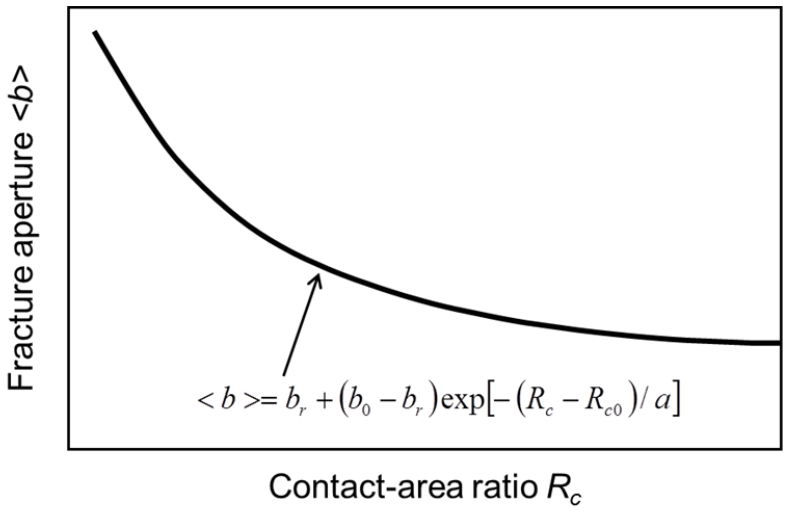

744

745 Fig. 2. Relation between fracture aperture and contact area ratio [11].

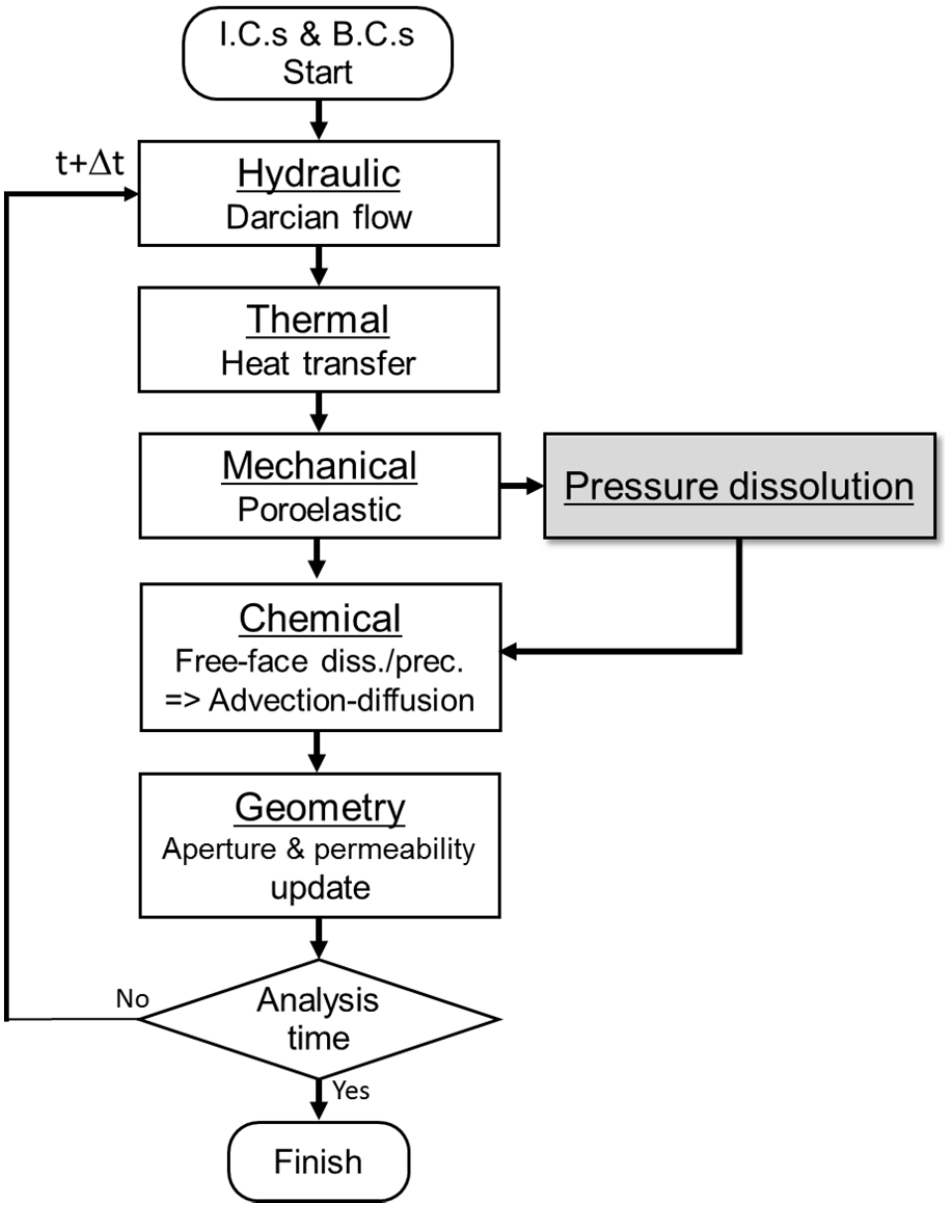

Fig. 3. Sequential procedure to conduct consistent calculations of aperture change with time. [Rev1.7]

761

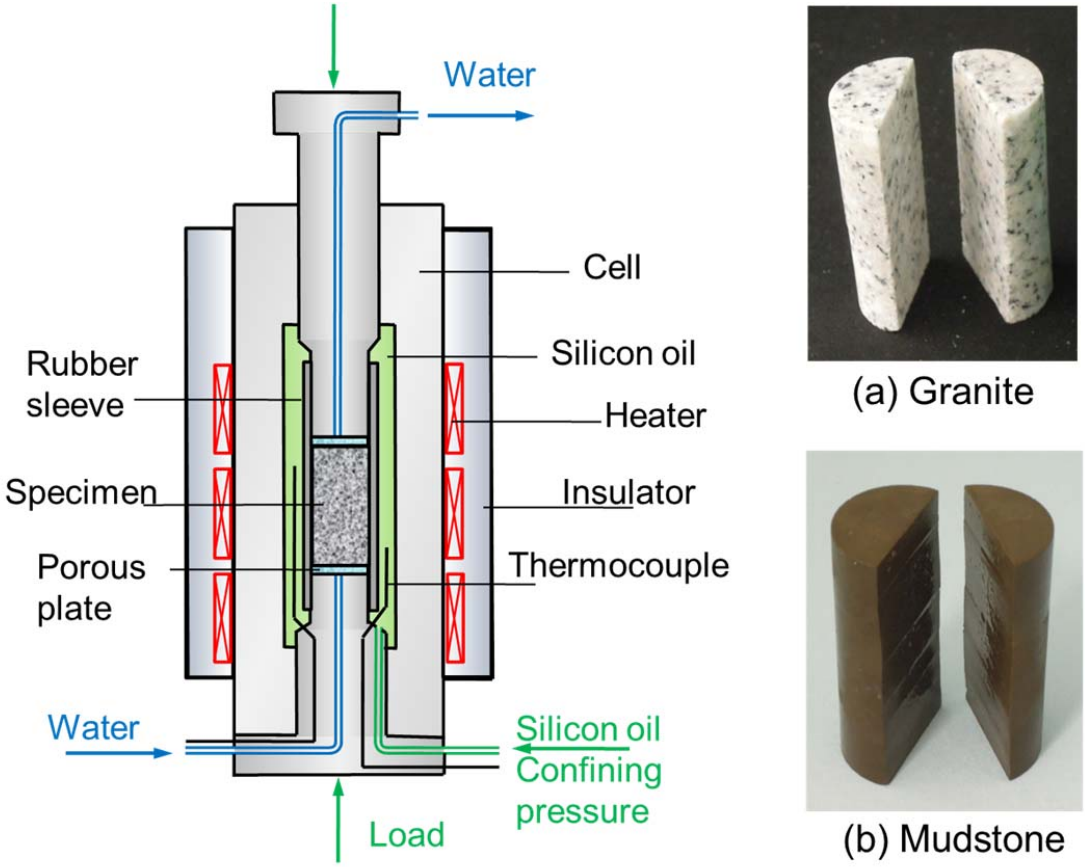

762

763

764 Fig. 4. Schematic of flow-through experiment (left side) and rock samples (right side) [11].

765

766

767

768

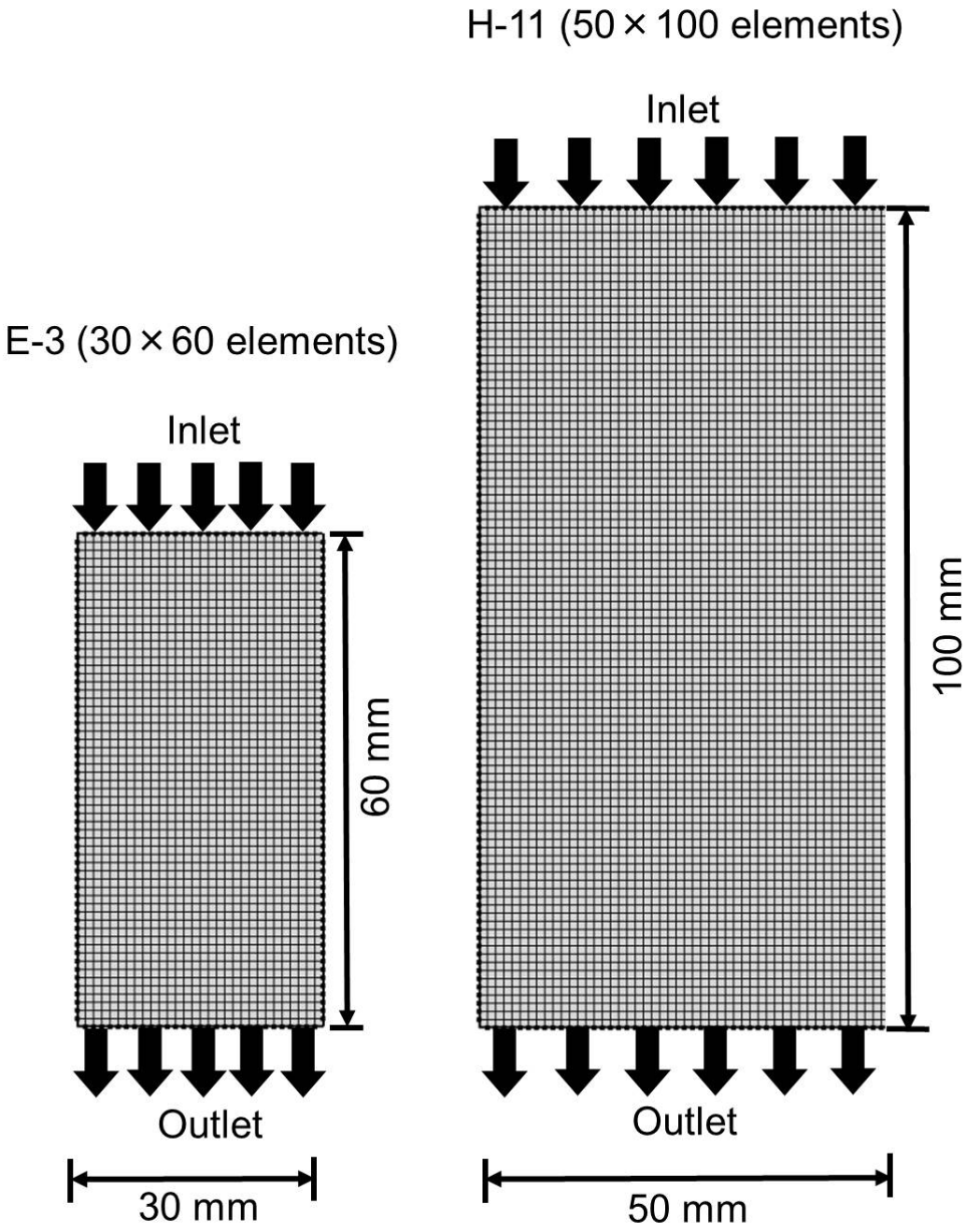

782 Fig. 5. Model geometry for analysis of E-3 and H-11. [(Re1.9), (Re2.5)]

783

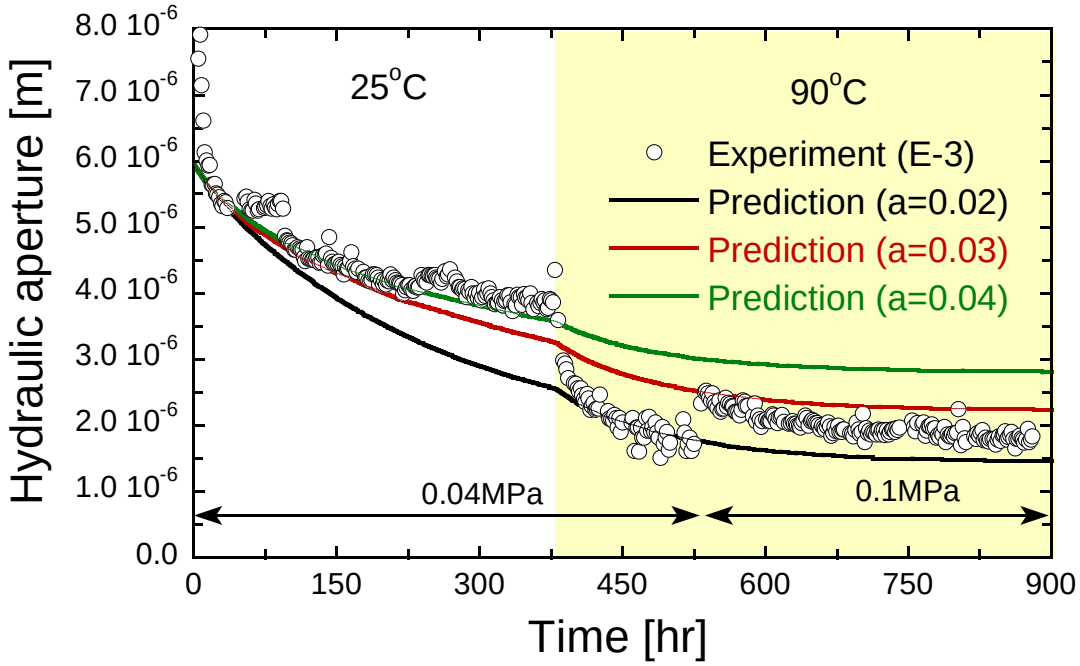

784

785

786 Fig. 6. Comparisons of evolution in fracture aperture (E-3) between measurements and

787 predictions with different values for *a* used in Eq. (30).

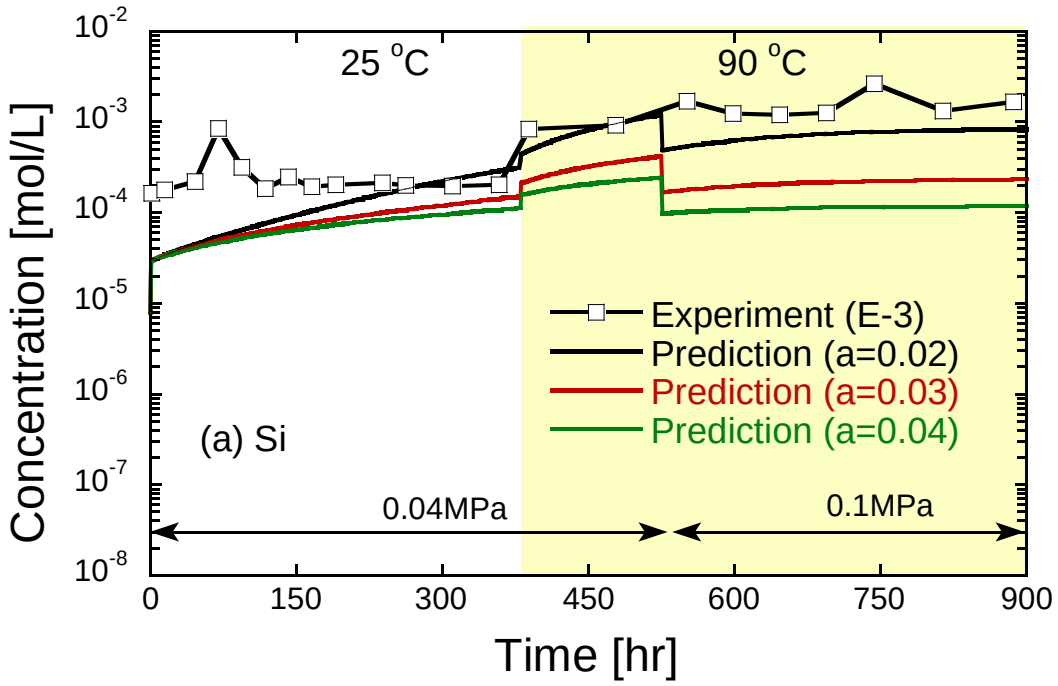

788

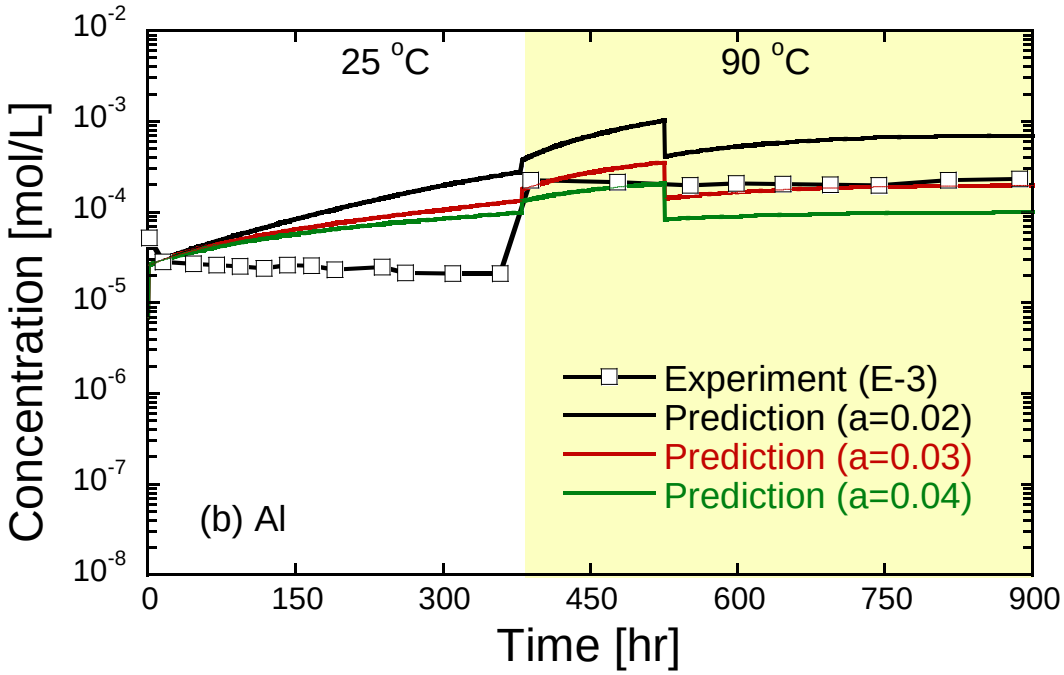

789

790

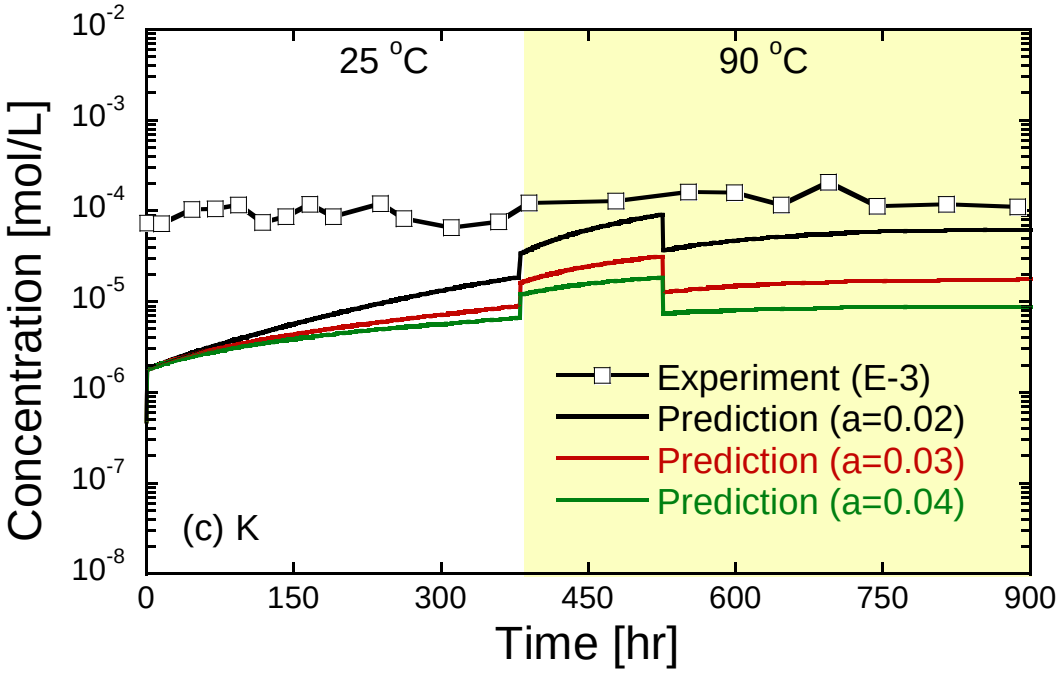

791

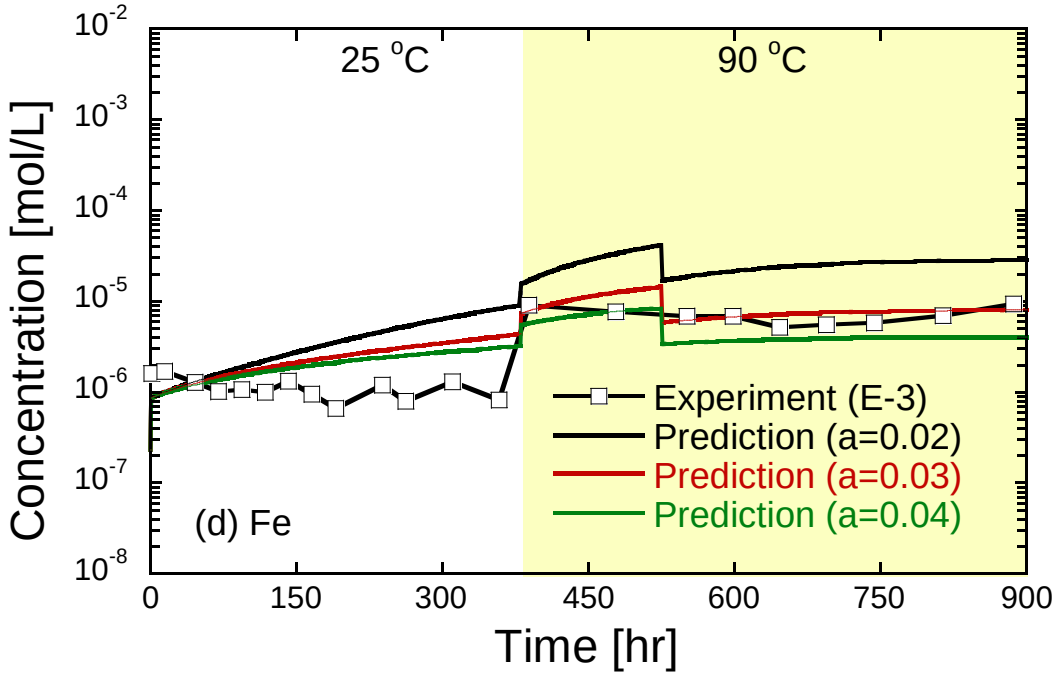

792

793

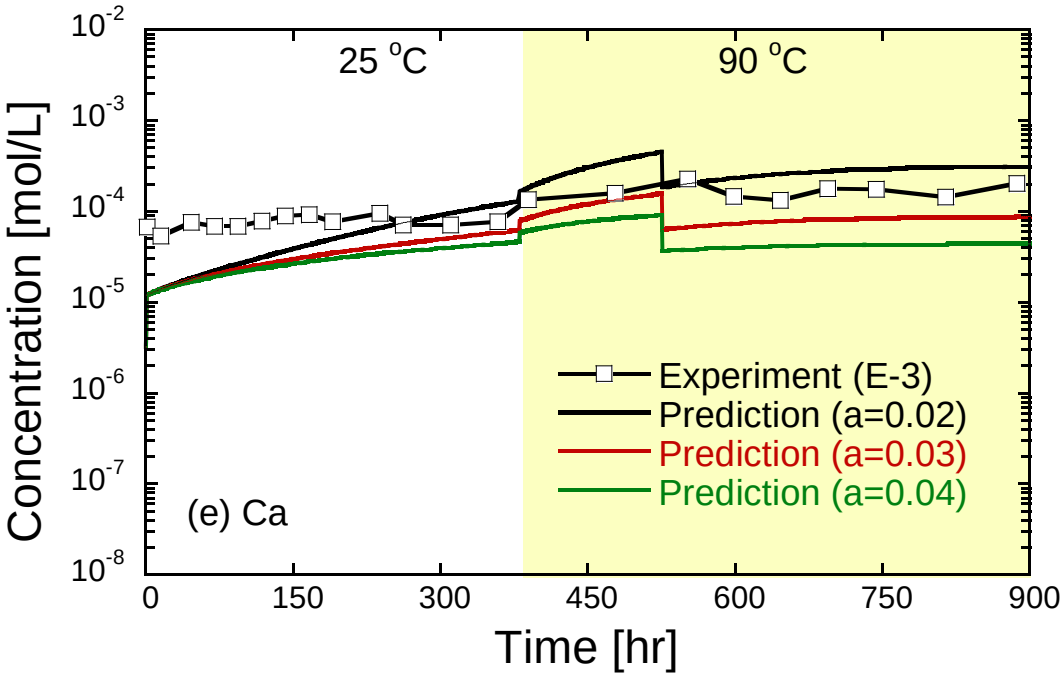

794

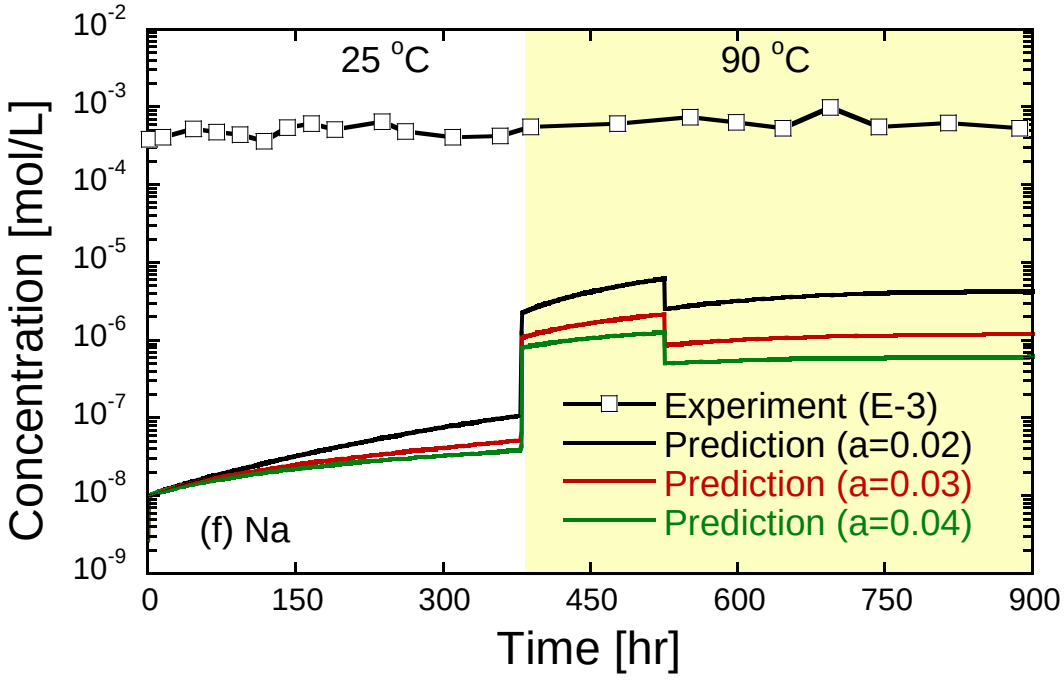

795

796

797

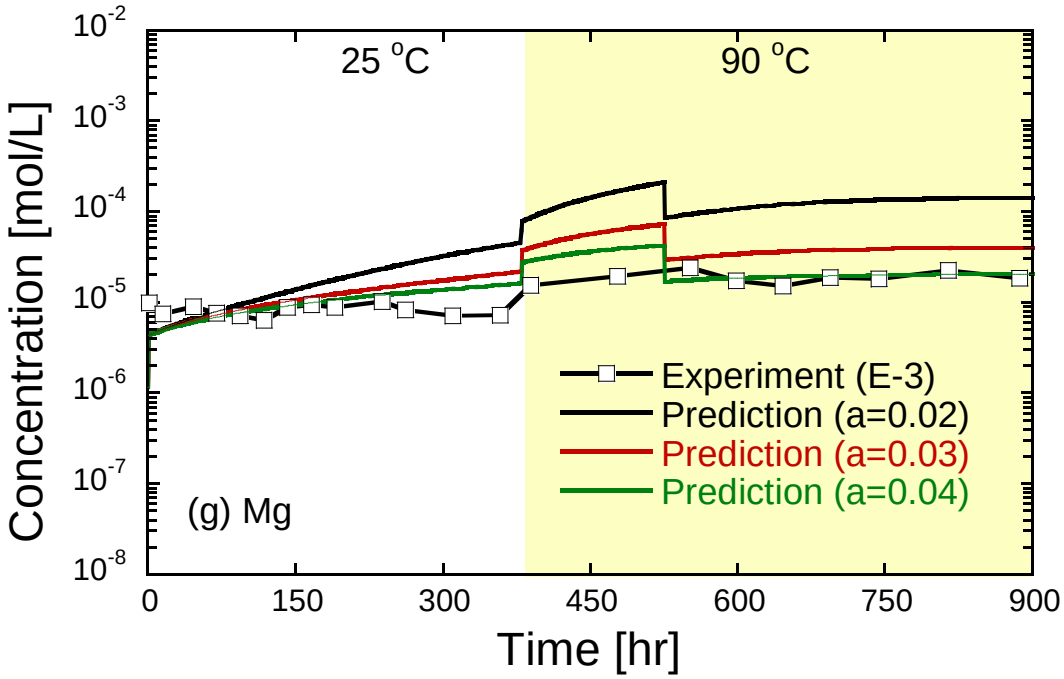

798

799 Fig. 7. Comparisons of element concentrations (E-3) between measurements and predictions with

800 different values for *a* used in Eq. (30) ((a) Si, (b) Al, (c) K, (d) Fe, (e) Ca, (f) Na, and (g) Mg).

801

802

803

804

805

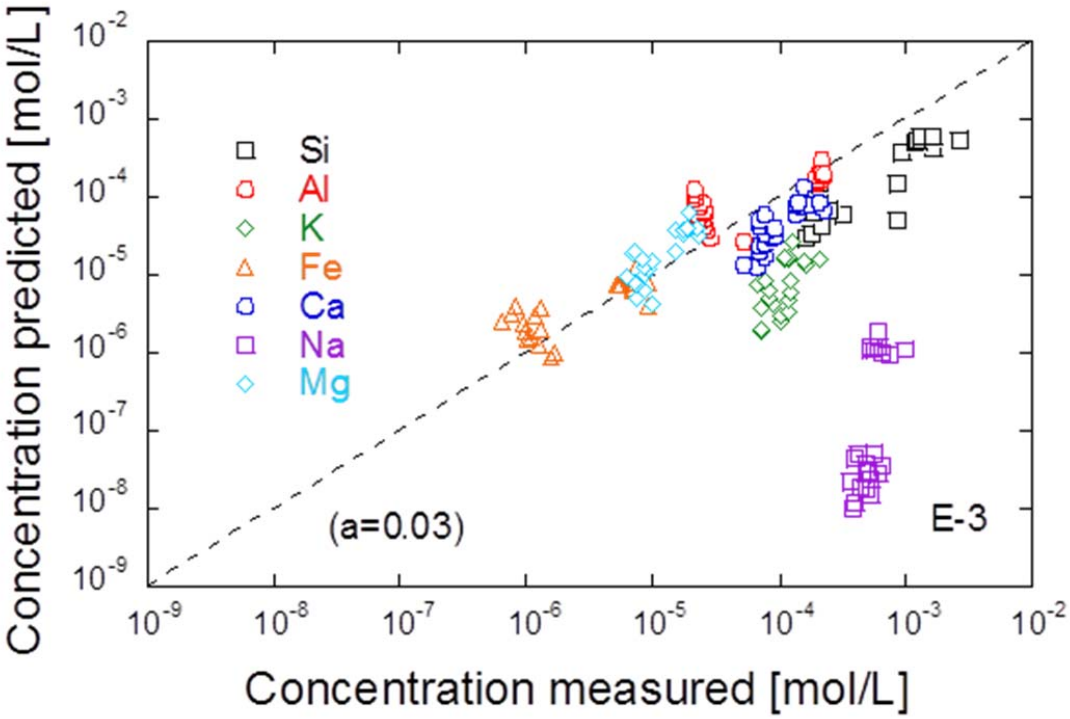

806

807 Fig. 8. Comparisons of element concentrations (E-3) between measurements and predictions with

808 a=0.03 used in Eq. (30)

809

810

811

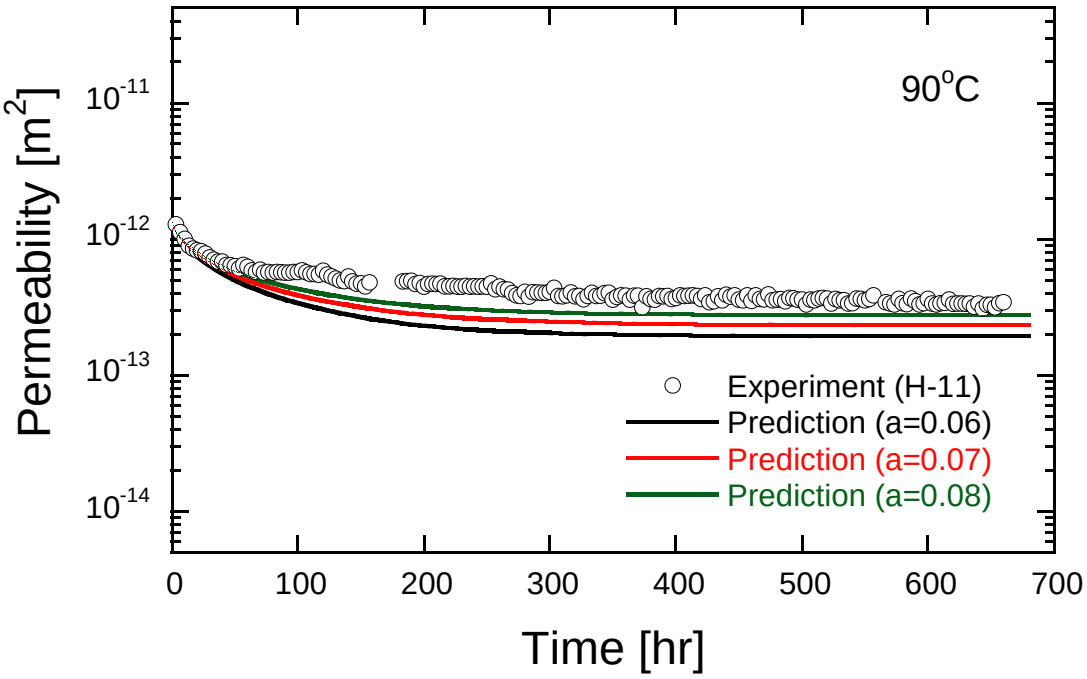

812

813 Fig. 9. Comparisons of evolution of fracture aperture (H-11) between measurements and

814 predictions with different values for *a* used in Eq. (30).

815

816

817

818

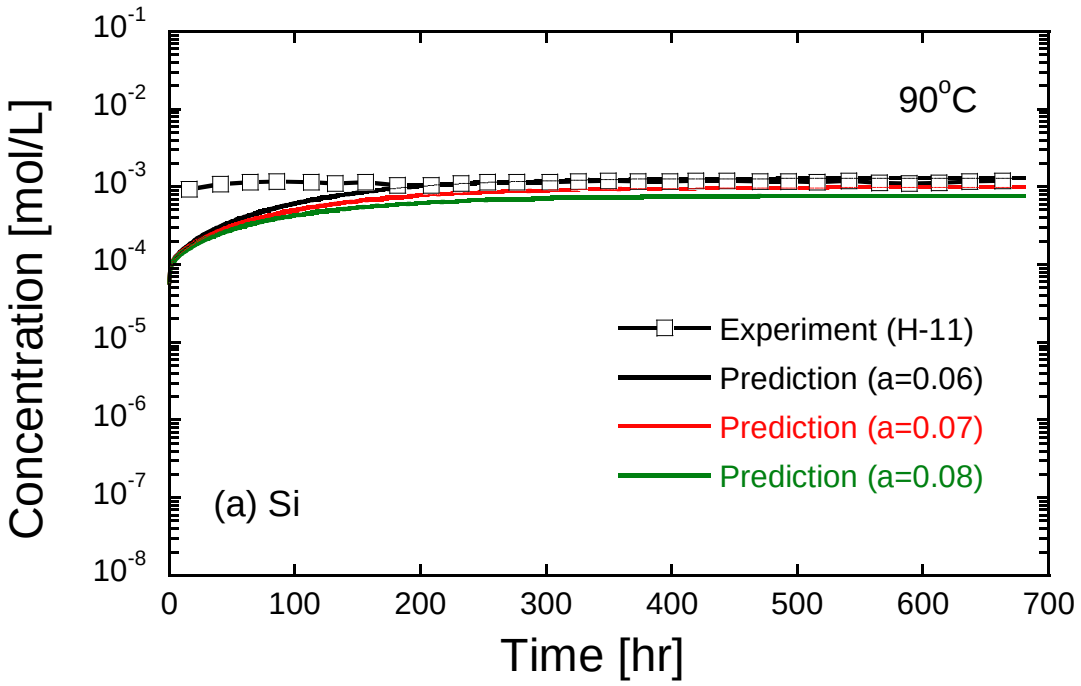

819

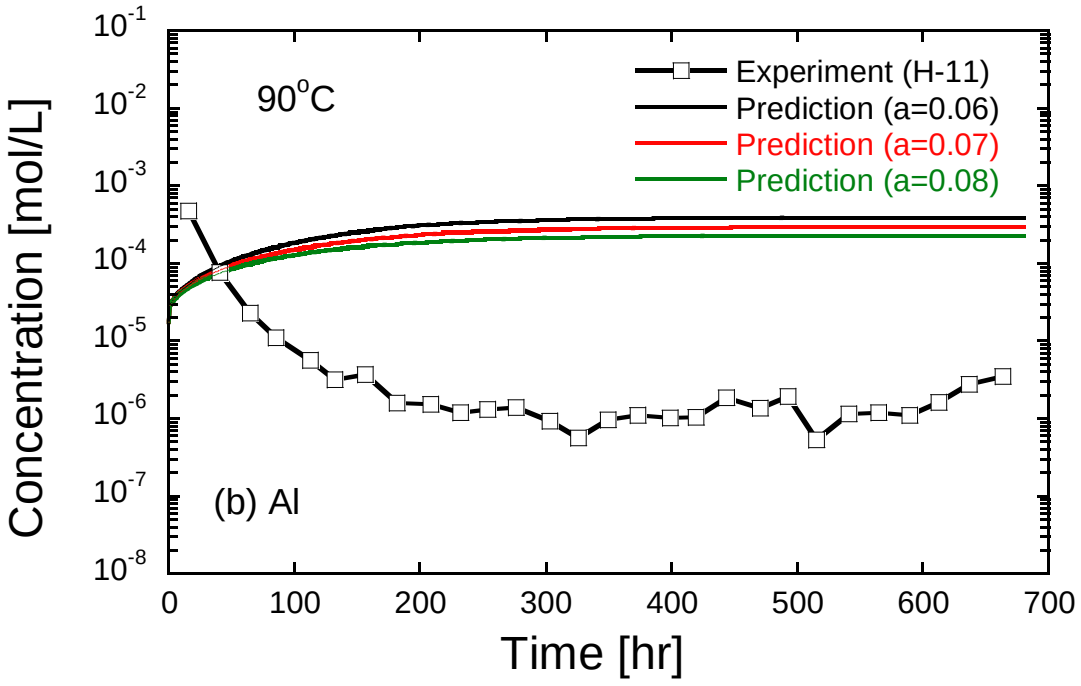

820

821

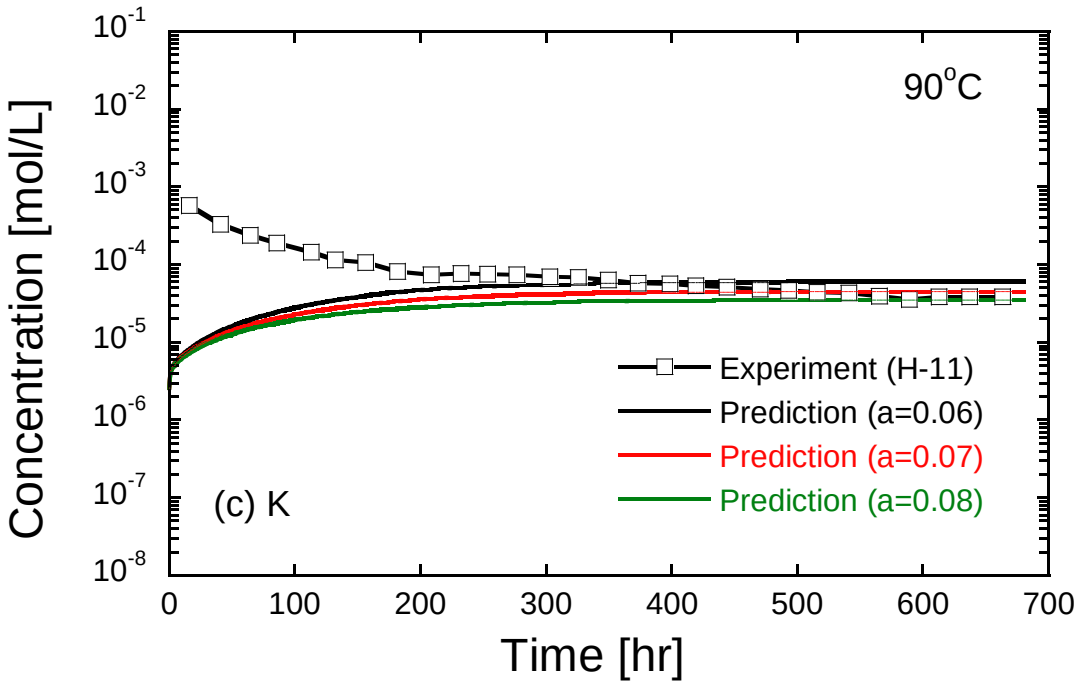

822

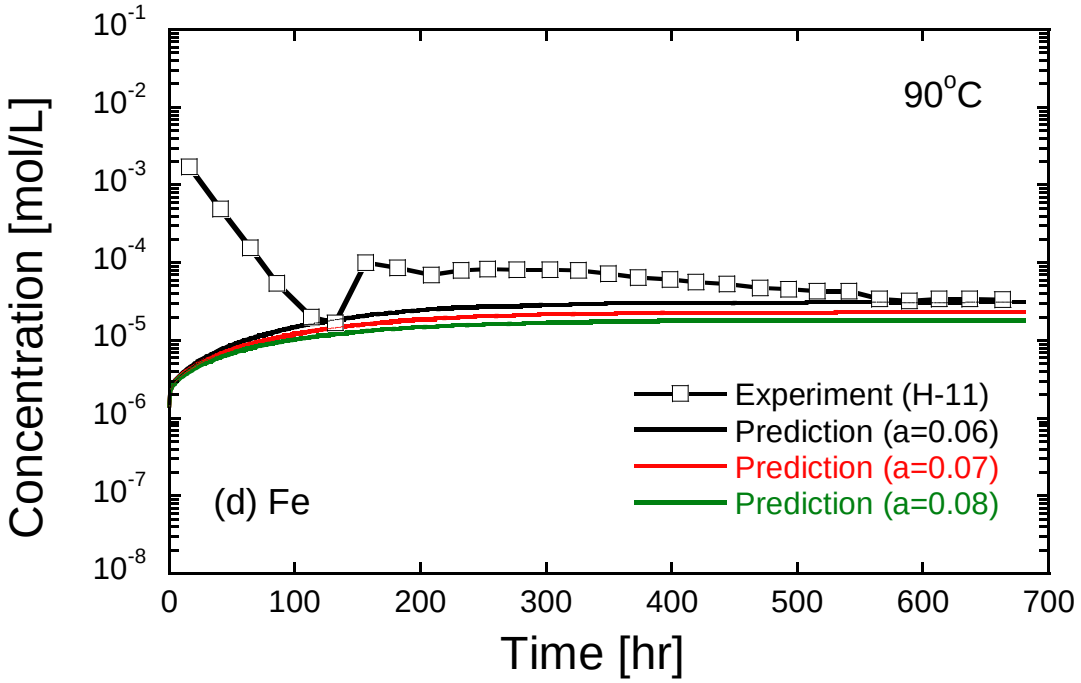

823

824

825

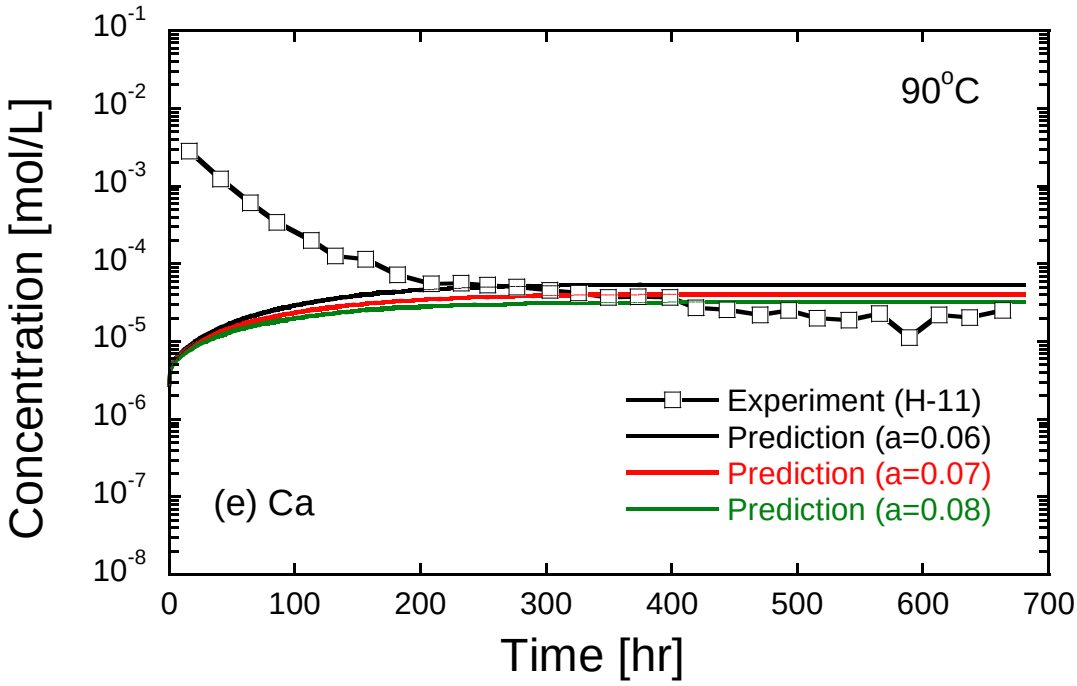

826

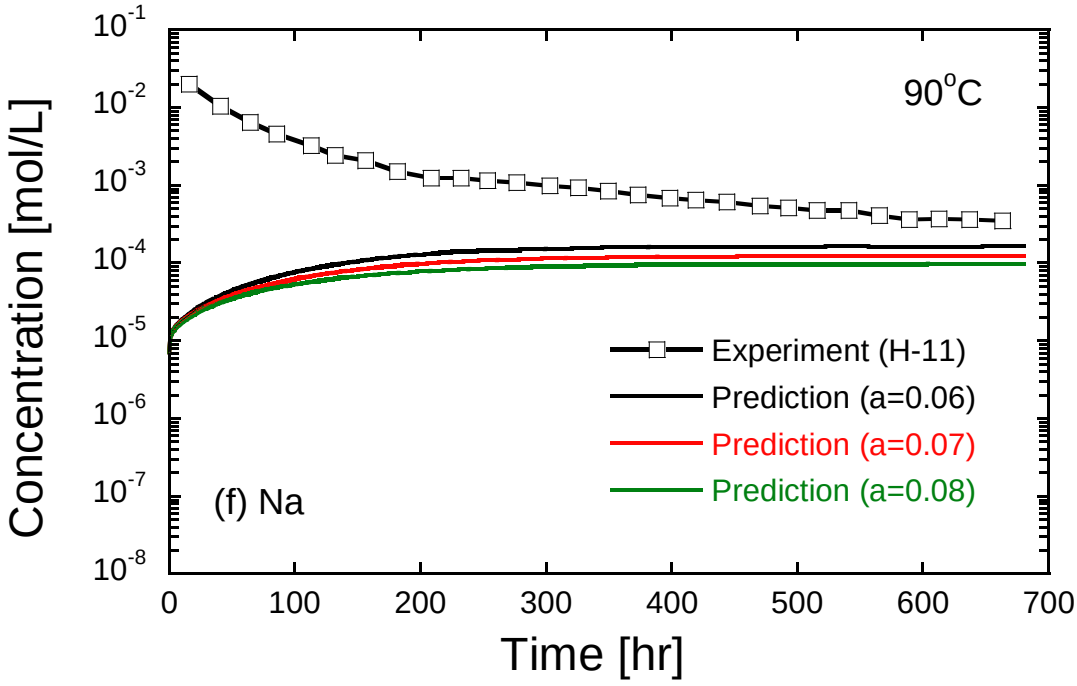

827

828

829

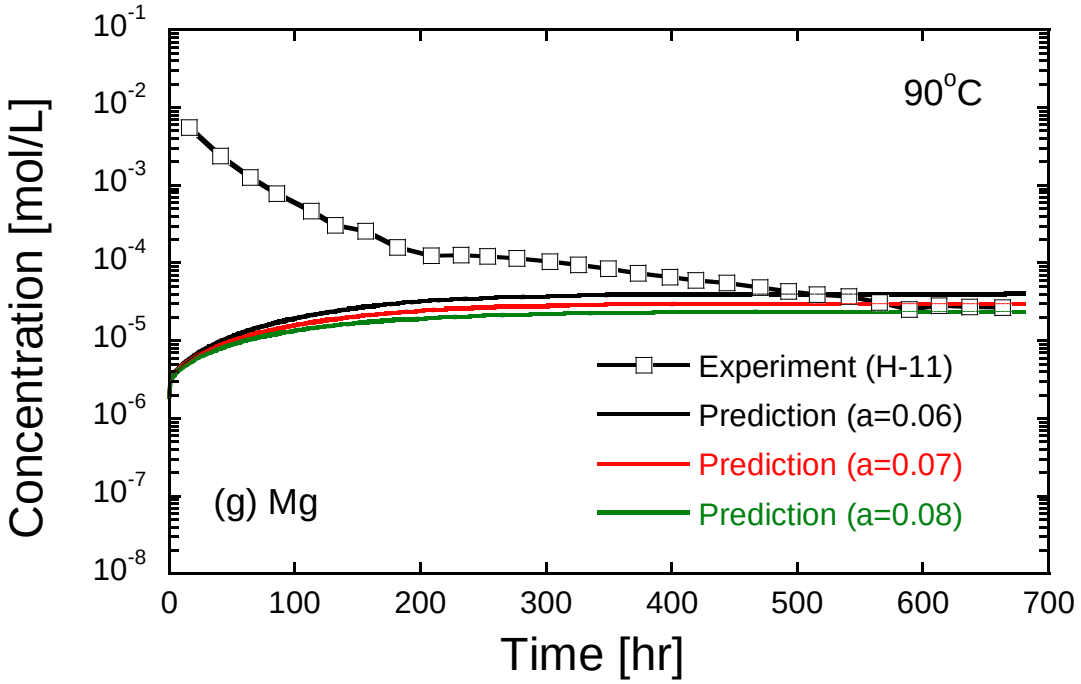

830

831 Fig. 10. Comparisons of element concentrations (H-11) between measurements and predictions

832 with different values for *a* used in Eq.(30) ((a) Si, (b) Al, (c) K, (d) Fe, (e) Ca, (f) Na, and (g)

833 Mg).

834

835

836

837

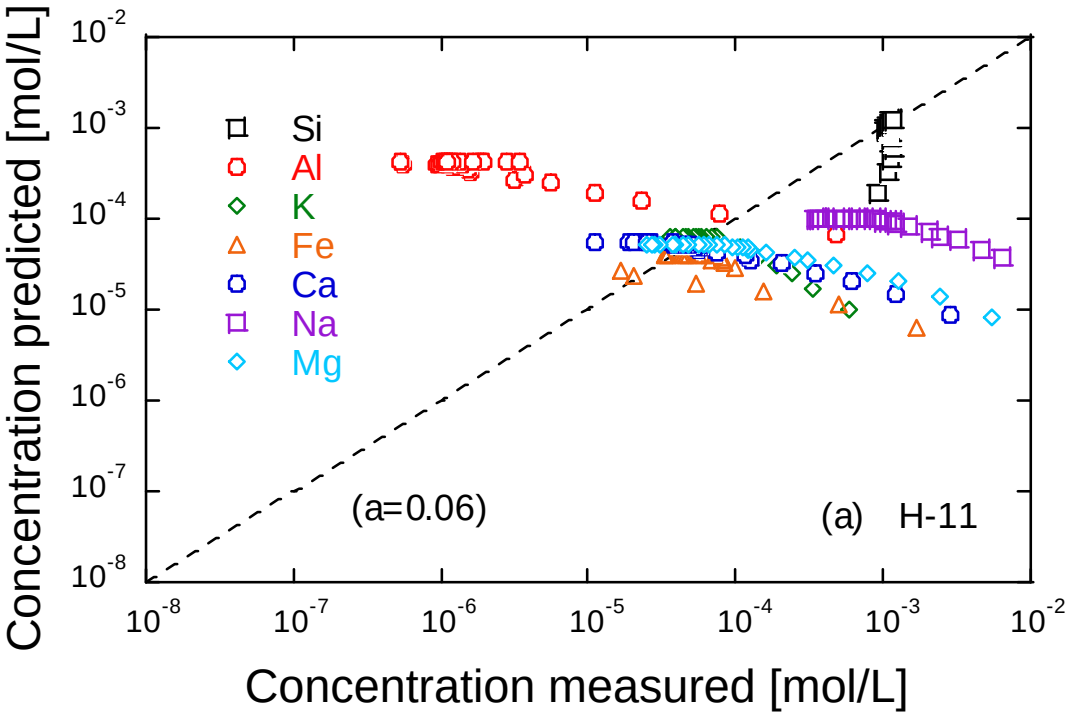

838

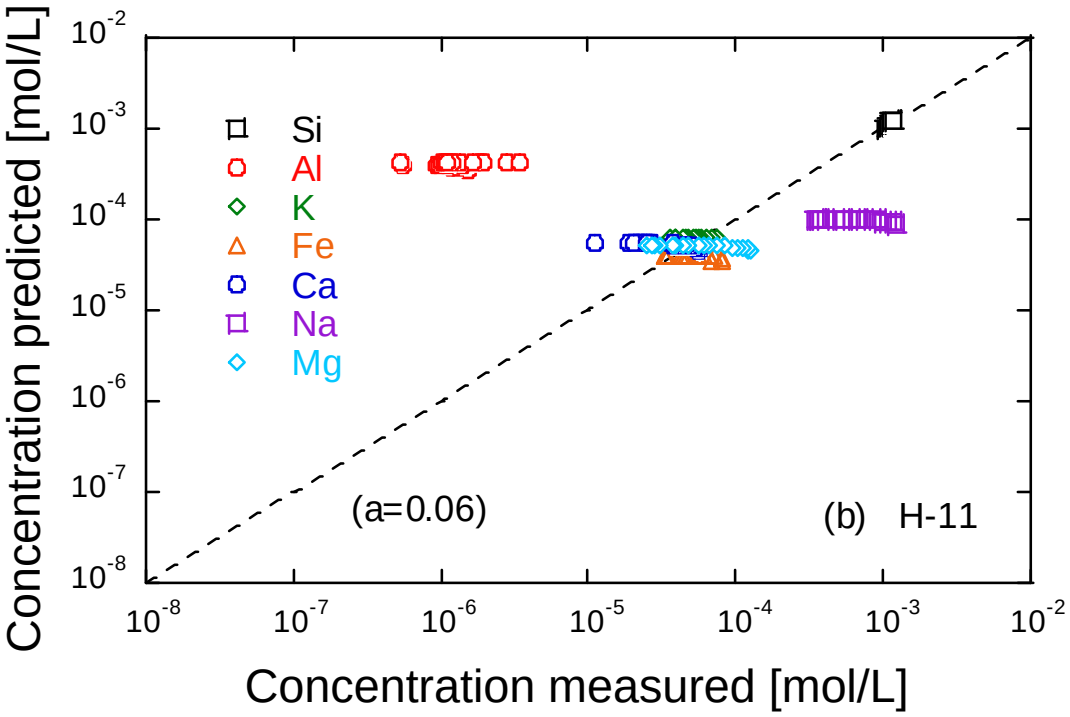

839

840 Fig. 11. Comparisons of element concentrations (H-11) between measurements and predictions

841 with a = 0.06 used in Eq. (30): (a) for whole experimental period and (b) for experimental period

842 after 200 h.